Chemical Engineering Science 195 (2019) 851–880

Contents lists available at ScienceDirect

Chemical Engineering Science

journal homepage: www.elsevier.com/locate/ces

Review

Diffusing uphill with James Clerk Maxwell and Josef Stefan

Rajamani Krishna

Van 't Hoff Institute for Molecular Sciences, University of Amsterdam, Science Park 904, 1098 XH Amsterdam, the Netherlands

HIGHLIGHTS

- Chemical potential gradients are the appropriate driving forces for diffusion.
- The Maxwell-Stefan formulation provides a unified description of diffusion.
- Diffusional coupling effects are strong near phase transition regions.
- Diffusional coupling often causes uphill transport and transient overshoots.
- Uphill diffusion is important in a wide variety of separation technologies.

ARTICLE INFO

Article history:
Received 9 April 2018
Received in revised form 25 September 2018
Accepted 22 October 2018
Available online 24 October 2018

Keywords:
Phase transitions
Coupled diffusion
Transient overshoots
Serpentine trajectories
Asymmetrical kinetics
Thermodynamic non-idealities
Electro-neutrality

ABSTRACT

The accurate description of molecular diffusion is important in the design and development of several processes of interest to chemical engineers. Most commonly, a component diffuses down the gradient of its concentration, and Fick's law provides an adequate description for calculation of the fluxes. The major objective of this review article is to highlight a wide variety of processes in which a component is transported uphill, requiring more rigorous models for describing diffusion.

Uphill diffusion may occur in multicomponent mixtures in which the diffusion flux of any species is strongly coupled to that of partner species. Such coupling effects often arise from strong thermodynamic non-idealities; for a quantitative description we need to use the Maxwell-Stefan formulation with chemical potential gradients as driving forces. Thermodynamic non-idealities are of particular significance for operations close to phase transition regions. A careful and detailed analysis of multicomponent distillation, and extraction processes reveals that Murphree component efficiencies could be "unbounded", i.e. exhibit values less than zero or exceed unity. A characteristic signature of uphill diffusion is the occurrence of transient overshoots in the approach to steady-state; the equilibration trajectories in composition space follow serpentine trajectories. For mixtures of liquids, metals, alloys, ceramics and glasses the serpentine equilibration trajectories could cause forays into meta-stable composition zones; such forays could result in spontaneous emulsification, and the Ouzo effect.

The transport of ionic species is invariably coupled with its partner ions because of the electroneutrality constraints; such constraints may accelerate or decelerate a specific ion resulting in uphill transport. The forward and reverse kinetics of uptake in ion-exchange resins are asymmetric.

For mixture separations with microporous adsorbents, uphill diffusion can cause supra-equilibrium loadings to be achieved during transient uptake within crystals; this allows the possibility of overriding adsorption equilibrium for achieving difficult separations.

Contents

E-mail address: r.krishna@contact.uva.nl

https://doi.org/10.1016/j.ces.2018.10.032
0009-2509/

Notation

a_i	component activity, dimensionless
$[B]$	matrix of inverse M−S coefficients, m^{-2} s
c_i	molar concentration of species i, mol m^{-3}
c_t	total molar concentration of mixture, mol m^{-3}
c_{fixed}	molar concentration of fixed charges in ion exchanger particle, equiv m^{-3}
d	bubble or droplet diameter, m
$Đ_i$	ion diffusivity, m^2 s^{-1}
$Đ_i$	diffusivity characterizing molecule-wall interactions, m^2 s^{-1}
$Đ_{ij}$	M−S binary pair diffusivity, m^2 s^{-1}
$[D]$	Fick diffusivity matrix, m^2 s^{-1}
E_i	component Murphree efficiency, dimensionless
F	Faraday constant, 9.65×10^4C mol^{-1}
Fo	Fourier number, dimensionless
$[I]$	identity matrix, dimensionless
J_i	molar diffusion flux of species i with respect to u, mol m^{-2} s^{-1}
M_i	molar mass of species i, kg mol^{-1}
n	number of species in the mixture, dimensionless
N_i	molar flux of species i in laboratory fixed reference frame, mol m^{-2} s^{-1}
N_t	molar flux of total mixture in laboratory fixed reference frame, mol m^{-2} s^{-1}
p_i	partial pressure of species i in mixture, Pa
p_t	total system pressure, Pa
$[Q]$	matrix quantifying fractional departure from equilibrium, dimensionless
R	gas constant, 8.314 J mol^{-1} K^{-1}
t	time, s
T	absolute temperature, K
x_i	mole fraction of component i in bulk fluid phase, dimensionless
X_i	ionic equivalent fraction of species i inside IEX particle, dimensionless
y_i	mole fraction of component i in bulk vapor phase, dimensionless
u	molar average mixture velocity, m s^{-1}
z	direction coordinate, m

Greek alphabet

β	cell constant, m^{-2}
γ_i	activity coefficient of component i, dimensionless
δ	length of diffusion path, m
δ_{ij}	Kronecker delta, dimensionless
$[\Gamma]$	matrix of thermodynamic factors, dimensionless
$[\Lambda] = [B]^{-1}$	matrix defined by Eq. (8), m^2 s^{-1}
μ_i	molar chemical potential, J mol^{-1}
ρ	framework density of adsorbent, kg m^{-3}
σ	rate of entropy production, J m^{-3} s^{-1} K^{-1}
Φ	electrostatic potential, V
ω_i	mass fraction of component i, dimensionless
ϕ_i	volume fraction of i in polymer solution, dimensionless

Subscripts

c	critical property
i	referring to component i
n	referring to component n
t	referring to total mixture

Matrix notation

( )	column matrix
[ ]	square matrix

1. Introduction

Fick's law, that relates the molar diffusion flux, J, to the composition gradient

$$J = -c_t D \frac{dx}{dz} \tag{1}$$

is widely used in chemical engineering practice in the modeling and design of process equipment. The Fick diffusivity is usually positive definite, i.e. $D > 0$, and the flux is directed down its composition gradient. However, Eq. (1) fails, even at a qualitative level, to describe the experimentally observed characteristics of mixture diffusion in a number of examples discussed hereunder.

Fig. 1a shows experimental data on the transient approach to equilibrium of He(1)/N_2(2)/CO_2(3) gas mixtures with different initial compositions in the two bulbs A, and B that are connected by a capillary tube. Particularly noteworthy is that the initial compositions of nitrogen in the two bulbs are identical but this does not prevent N_2 from diffusing between the two bulbs, exhibiting overshoots and undershoots in its approach to thermodynamic equilibrium. Fig. 1b shows the transient approach to equilibrium in a two-bulb diffusion apparatus with different initial compositions of the ternary H_2(1)/N_2(2)/CO_2(3) gas mixture in the two bulbs. Also for this mixture, N_2 exhibits overshoots and undershoots in its approach to thermodynamic equilibrium, even though there is no driving force for nitrogen at time $t = 0$. The use of Eq. (1) would anticipate no diffusion of nitrogen for the examples in Fig. 1a and b.

The experimental data for transient equilibration of CH_4(1)/Ar (2)/H_2(3) gas mixtures in a Loschmidt tube experiment with different initial compositions in the top and bottom compartments are

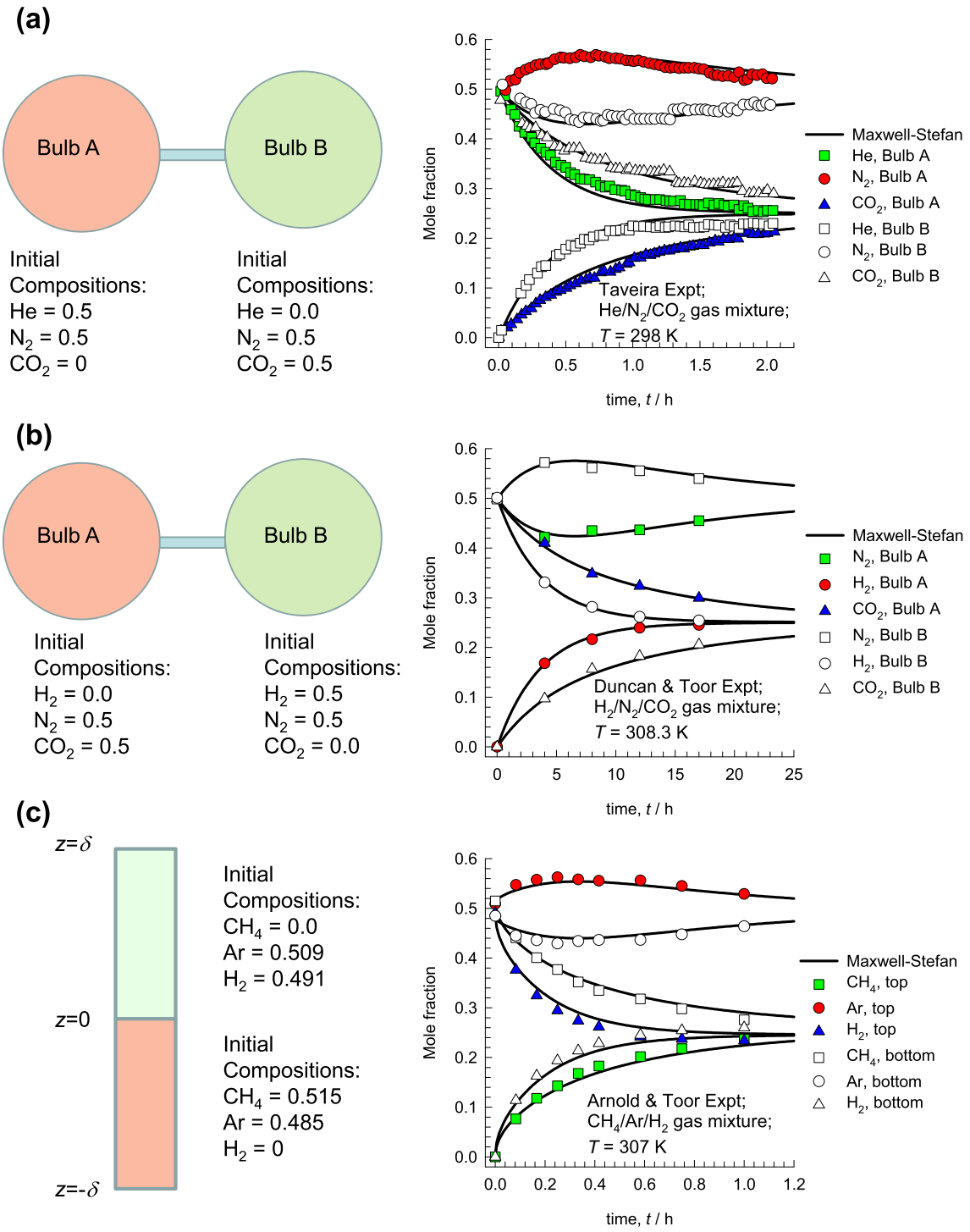

Fig. 1. (a) Experimental data of (Taveira et al., 2000) on the transient approach to equilibrium in the two-bulb diffusion experiments for He(1)/N_2(2)/CO_2(3) mixtures at p_t = 40 kPa, and T = 298 K. (b) Experimental data of (Duncan and Toor, 1962) on the transient approach to equilibrium in the two-bulb diffusion experiments for H_2(1)/N_2(2)/CO_2(3) mixtures at p_t = 101.3 kPa, and T = 308.3 K. (c) The Loschmidt tube experiment of (Arnold and Toor, 1967) on the transient approach to equilibrium for CH_4(1)/Ar(2)/H_2(3) gas mixtures at p_t = 101.3 kPa, and T = 307 K. The plotted data are spatially-averaged compositions in the two cylinders. The continuous solid lines are the solutions to the Maxwell-Stefan equations. Modeling and computational details are provided in Chapter 3 of the Supplementary Material.

shown in Fig. 1c. Argon shows transient overshoots (top compartment) and undershoots (bottom compartment) in its approach to equilibrium. The occurrence of overshoots and undershoots in Fig. 1a–c signals uphill diffusion and the attainment of supra-equilibrium compositions during a finite time interval in the transient equilibration process. The modeling of uphill diffusion would require the Fick diffusivity of that component to assume negative values, i.e. $D < 0$, making its physical significance difficult to fathom.

Diffusion close to phase transition regions is of importance in a wide variety of processes such as liquid extraction, crystallization, and precipitation. In the experiments of (Krishna et al., 1985), two different compositions A and B of partially miscible ternary mixture glycerol(1)/acetone(2)/water(3) mixtures were brought into

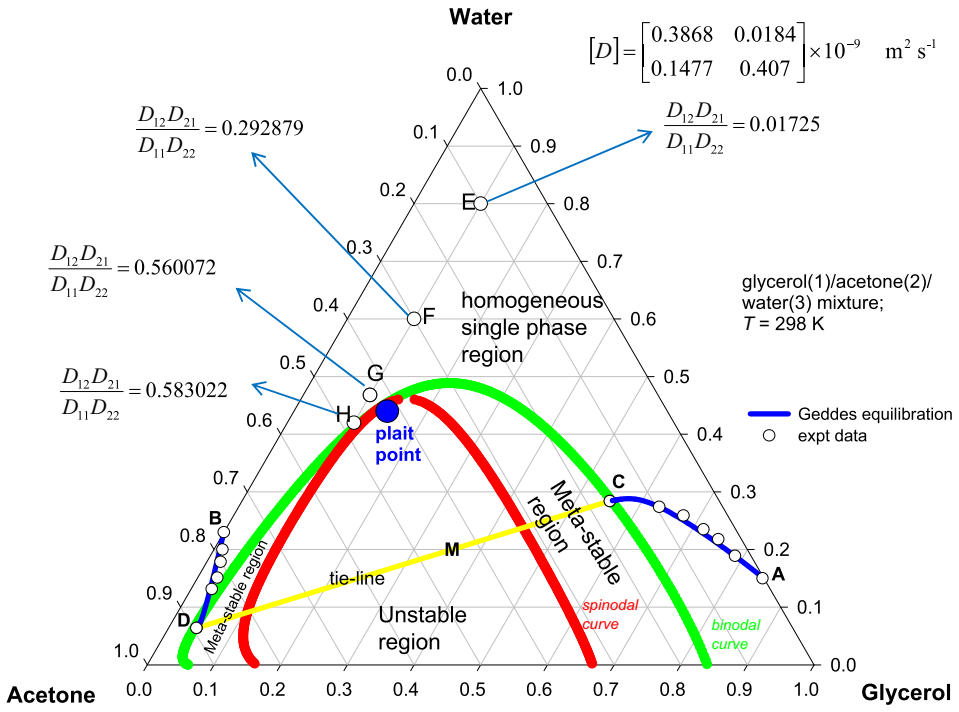

Fig. 2. Schematic showing liquid/liquid phase equilibrium for glycerol(1)/acetone(2)/water(3) mixtures at 298 K. The binodal and spinodal curves converge at the plait point. The two mixtures of compositions A and B are brought into contact in a stirred Lewis cell (Krishna et al., 1985). The average mixture composition (M) falls within in the two-phase region. The mixture with a composition M will split into two phases at either end of the tie-line. Each of the mixtures A and B will equilibrate to the compositions at the two ends of the tie-line connecting C and D. Also indicated are the four different compositions, E, F, G, and H for which (Grossmann and Winkelmann, 2005, 2007a,b) have measured the Fick diffusivity matrix [D] for glycerol(1)/acetone(2)/water(3) mixtures. The spinodal curve is calculated using the constraint $|\Gamma|$=0. Modeling and computational details are provided in Chapter 6 of the Supplementary Material.

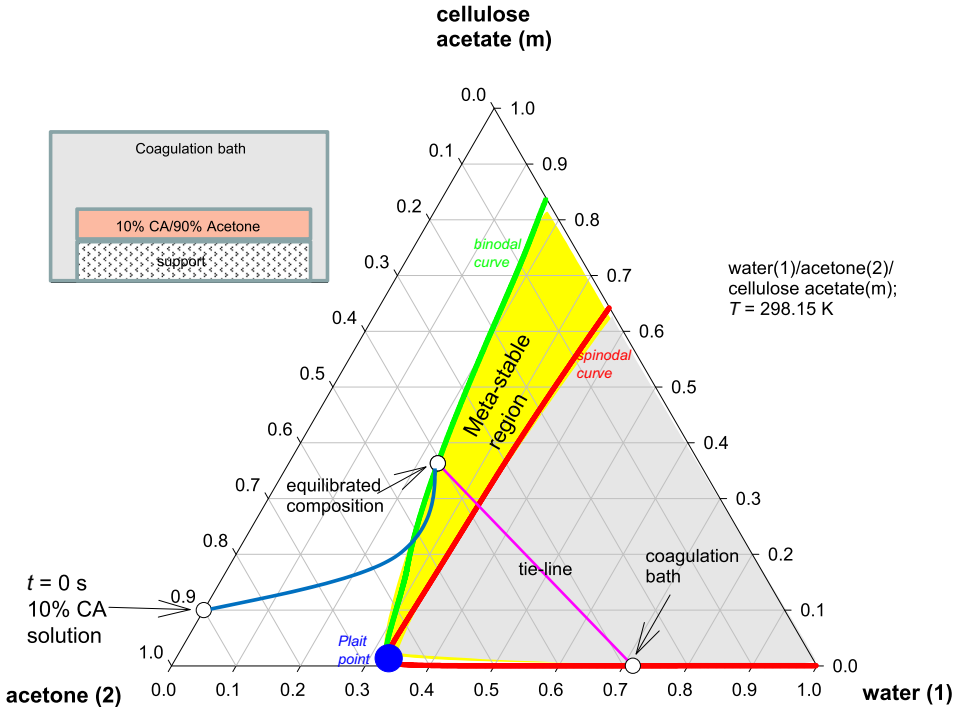

Fig. 3. Diffusion trajectories during the immersion precipitation process for membrane preparation; adapted from the papers of (Reuvers and Smolders, 1987; van den Berg and Smolders, 1992) A 10% solution of Cellulose Acetate (CA) in acetone is immersed in a bath of pure water. The transient equilibration trajectory is indicated in a qualitative manner.

contact in a stirred Lewis cell; see Fig. 2. The average mixture composition (M) falls within the two-phase region. Each of the mixtures A and B will equilibrate to the compositions at the two ends of the tie-line corresponding to the mixture composition M; these compositions (C, and D) are different from those of A and B. The experimentally determined equilibration trajectories A–C,

and B–D are found to be strongly curvilinear. If the simple Fickian Eq. (1) is employed to model the equilibration process, with the assumption of concentration-independent diffusivities, both the equilibration trajectories in Fig. 2 would be linear.

Curvilinear diffusion equilibration trajectories for water/acetone/cellulose acetate mixtures have also been reported in the preparation of cellulose acetate membranes by the process of immersion precipitation (Krishna, 2016e, 2017b; Reuvers and Smolders, 1987; Tsay and McHugh, 1990; van den Berg and Smolders, 1992). Fig. 3 shows the transient equilibration trajectory when a 10% solution of Cellulose Acetate (CA) in acetone is immersed in a coagulation bath containing aqueous solution of acetone. We note the curvilinear trajectory has entered the meta-stable region. This foray into the meta-stable region impacts on the membrane structure. What causes the equilibration process to follow a circuitous path to equilibrium, via the meta-stable region?

Ion exchange processes are commonly carried out in fixed bed device, and operated in transient mode, with adsorption and regeneration cycles (Seader et al., 2011). A cation exchange particle, for example, consists of fixed negative charges (e.g. HSO_3^-) on a polymer matrix; see schematics in Fig. 4a,b. Positively charged *counter*-ions such as H^+, Na^+, Ba^{++}, Zn^{++} and Cs^+ can exchange between the IEX particle and the surrounding bulk electrolyte liquid, but *co*-ions such as Cl^-, SO_4^{-2}, and NO_3^- are virtually excluded from participation in the forward/reverse exchanges. Fig. 4c shows the experimental data for transient uptake of H^+/Zn^{++} into a DOWEX 50WX10 cation exchanger that is initially loaded with Na^+. Supra-equilibrium loadings of H^+ are realized during the early stages of transience; the transient overshoot in the uptake of H^+ signals uphill diffusion. Remarkably, no overshoots are detected for the reverse ion exchange process in which the particle is initially loaded with H^+/Zn^{++} and is replaced by Na^+; see Fig. 4d. The asymmetry in the forward/reverse exchange processes is impossible to model by use of Eq. (1).

Fig. 5 shows experimental data on the transient uptake of $CO_2(1)/C_2H_6(2)$ mixtures in crystals of DDR, a cage-type zeolite with 3.65 Å X 4.37 Å windows. The tardier-more-strongly-adsorbed C_2H_6 approaches thermodynamic equilibrium in a monotonic manner. The more-mobile-less-strongly-adsorbed CO_2 displays a loading overshoot in its approach to equilibrium. The attainment of supra-equilibrium CO_2 loadings during the early transience is indicative of uphill diffusion of CO_2. Use of a simple Fickian model for intra-crystalline fluxes will anticipate monotonous equilibration of both components.

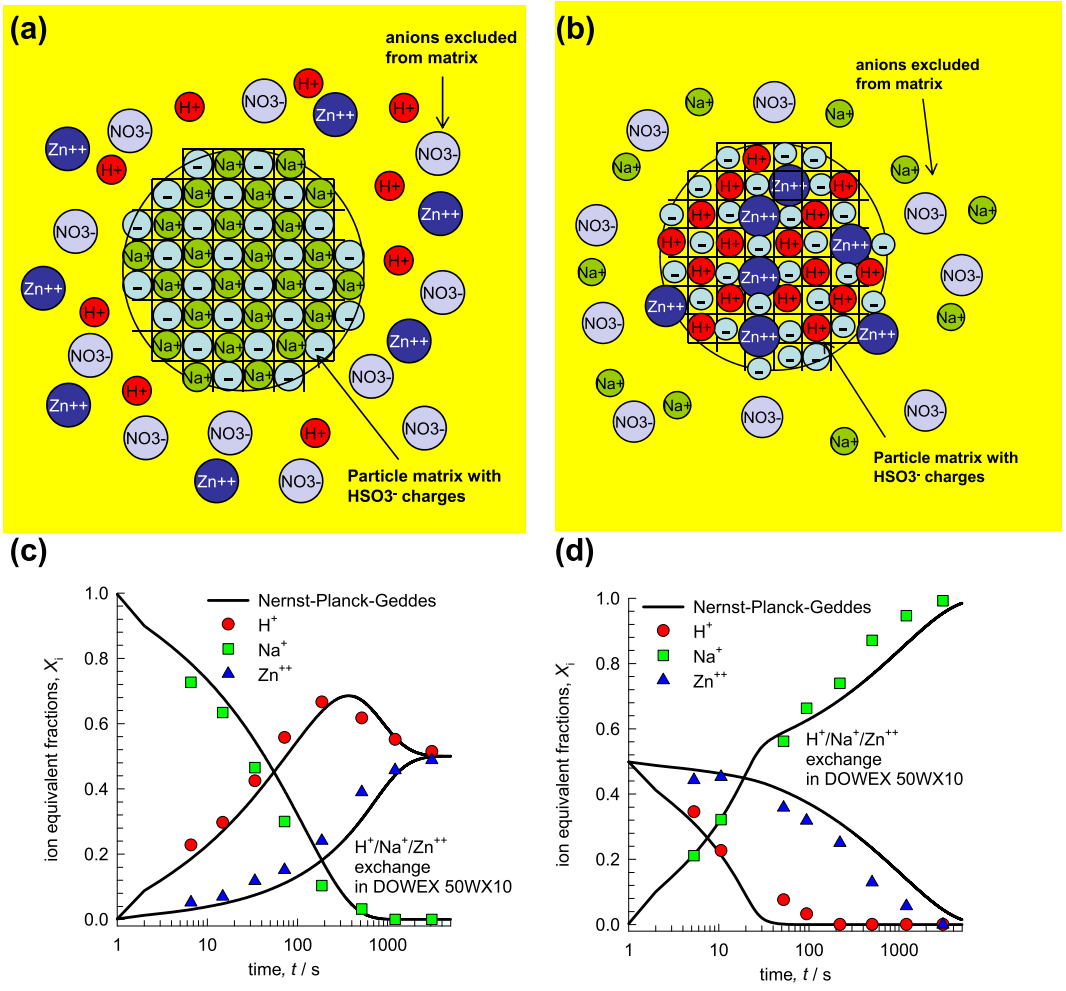

Fig. 4. (a) Schematic showing an ion exchanger particle with fixed $HSO3^-$ charges, and loaded with Na^+; the surrounding liquid phase consists of a solution of HNO_3 and $Zn(NO_3)_2$. The electrolytes are fully ionized and the bulk liquid phase contains H^+, Zn^{++}, NO_3^- ions along with unionized water molecules. (b) Schematic showing an ion exchanger particle with fixed $HSO3^-$ charges, and loaded with H^+, and Zn^{++}; the surrounding liquid phase consists of a solution of $NaNO_3$. (c, d) Transient exchange of $H^+/Na^+/Zn^{++}$ within DOWEX 50WX10 cation exchanger particle of radius 0.4 mm. Two scenarios are considered. (c) Initially the particle is loaded with Na^+ and is replaced H^+/Zn^{++}. (d) Initially the particle is loaded with H^+/Zn^{++} and is replaced Na^+. The experimental data in (Yoshida and Kataoka, 1987) are indicated by symbols. The Nernst-Planck-Geddes model simulations are indicated by the continuous solid lines. Modeling and computational details are provided in Chapter 10 of the Supplementary Material.

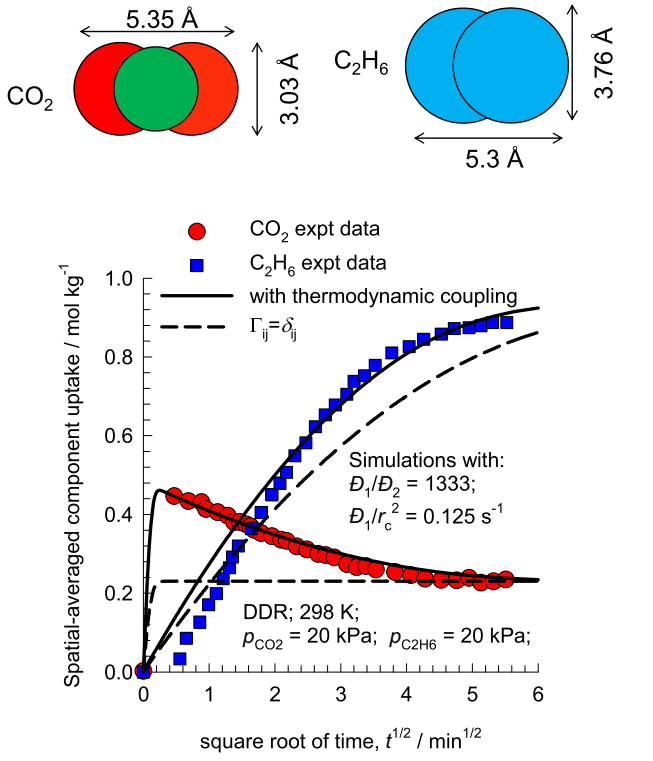

Fig. 5. Experimental data of (Binder et al., 2015; Lauerer et al., 2015) (indicated by symbols) for spatial-averaged transient uptake of 1:1 $CO_2(1)/C_2H_6(2)$ gas mixtures within crystals of DDR zeolite. The continuous solid lines are numerical simulations based on the flux Eq. (44). The dashed lines are the calculations using the simplification $\Gamma_{ij} = \delta_{ij}$. Modeling and simulation details are provided by (Krishna, 2016d, 2018).

(Sabatier and Vignes, 1967) and (Vignes and Sabatier, 1969) investigated inter-diffusion between the left and right compartments of Co(1)/Fe(2)/Ni(3) solid mixtures, annealed to a temperature of 1588 K. The initial atom fraction of Ni in the left and right bars are identical and equal 0.5. However, the absence of differences in the Ni compositions does not prevent transport of Ni, as evidenced by the data presented in Fig. 6 on the atom fractions measured at $t = 17$ h after the start of the experiment. The overshoot and undershoot of Ni are indicative of uphill transport.

In the classic experimental work of (Darken, 1949), two austenite bars of different compositions (0.48% C, 3.8% Si), and (0.45% C, 0.05% Si) are welded together. Carbon was allowed to diffuse for 13 days at 1323 K; after this period the bars are quenched and the composition profiles determined as shown in Fig. 7a. The high C content near the surface of the austenite bar on the right hand side, imparts the required "hardness" to steel. The process of hardening of steel by "carburizing" is reliant on uphill transport of carbon from the high-Si bar to the low-Si bar, despite the fact that the initial compositions of carbon are practically the same in the two adjoining bars. Darken recognized the need to use activity gradients as proper driving forces when setting up the phenomenological relations to describe diffusion. Carbon in the high-Si bar has a higher activity than the bar with the lower Si content; Fig. 7b shows the corresponding profiles of the activity of C; transport of C is down the gradient of the component activity.

Three quotes from (Darken, 1949) serve as tramlines for the ensuing discussions and analyses presented in this article:

> *"the driving force in an isothermal diffusion process may be regarded as the gradient of the chemical potential,",*

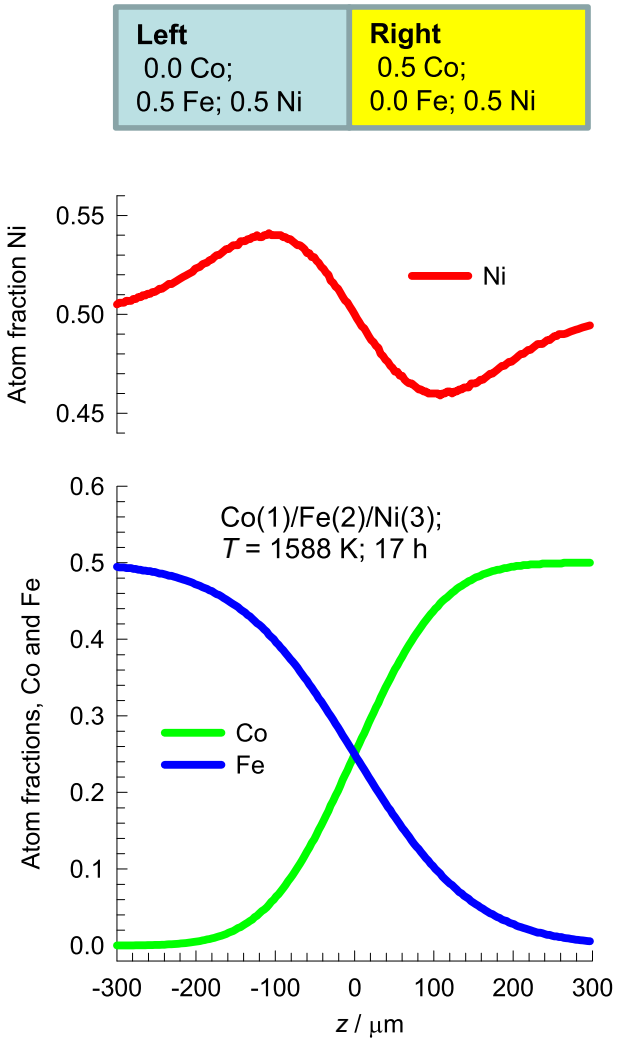

Fig. 6. (a) Simulations of transient inter-diffusion between the left and right compartments of Co/Fe/Ni mixture, annealed to a temperature of 1588 K. The atom fraction of each component on either side of the Matano plane, at $t = 17$ h after the start of the simulation are shown. (b) Equilibration trajectories in composition space. These simulations are designed to match the experimental data of (Sabatier and Vignes, 1967; Vignes and Sabatier, 1969). Modeling and computational details are provided in Chapter 8 of the Supplementary Material.

> *"for a system with more than two components it is no longer necessarily true that a given element tends to diffuse toward a region of lower concentration even within a single phase region", and*
>
> *"departure from the behavior of an ideal solution may be so great that the concentration gradient and the chemical potential gradient, or activity gradient, may be of different sign, thus giving rise to uphill diffusion".*

The primary objective of this review article is to highlight the widespread manifestation and significance of uphill diffusion in processes of significant importance to chemical engineers. We aim to show that the set of experiments shown in Figs. 1–7 can all be quantitatively modeled by adopting a common, and unified diffusion formulation. In keeping with earlier work (Krishna and Wesselingh, 1997), the approach we adopt to relate the chemical potential gradients to the component fluxes stems from the pioneering works of (Maxwell, 1866) and (Stefan, 1871). Essentially, the Maxwell-Stefan (M–S) equations represent a balance

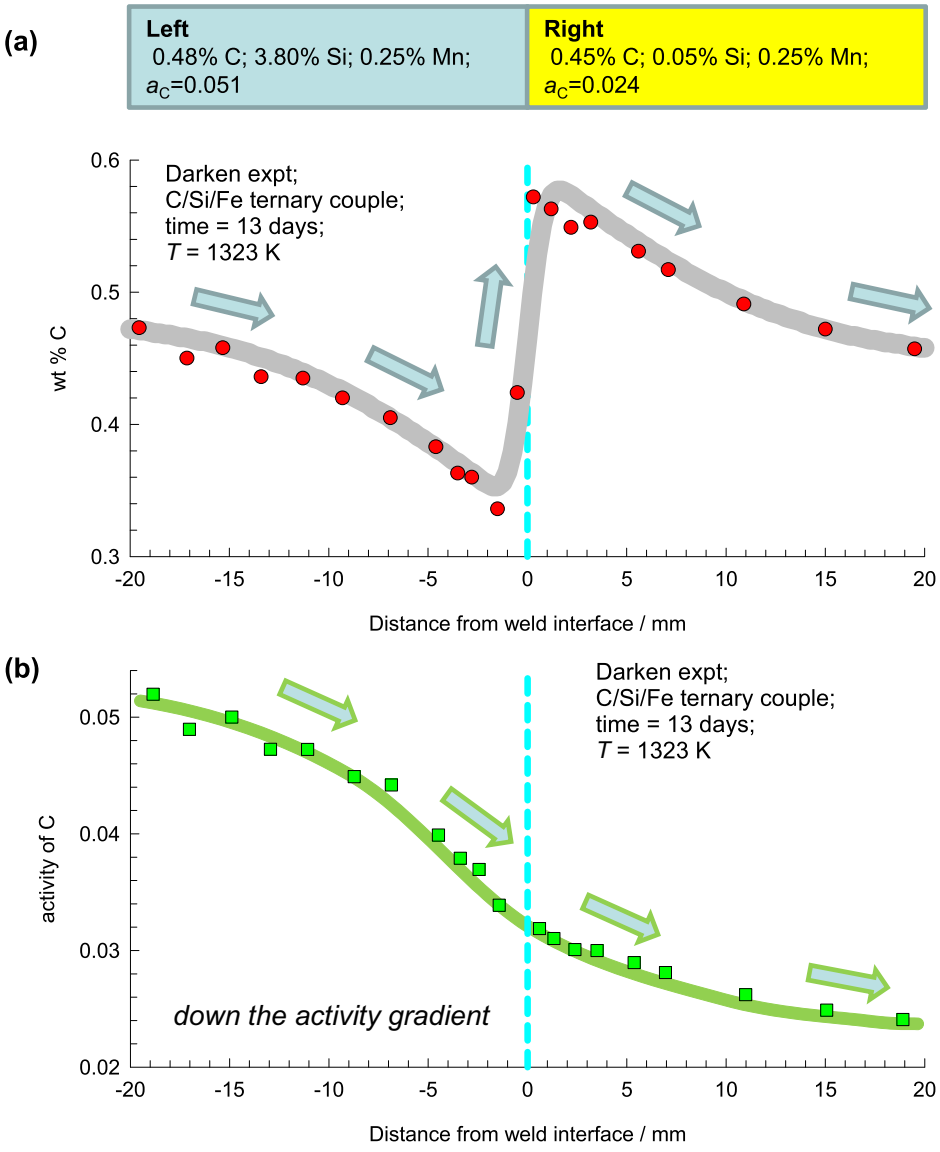

Fig. 7. (a) Experimental data of (Darken, 1949) for inter-diffusion between the left and right austenite bars consisting of C/Si/Fe mixtures, annealed to a temperature of 1323 K. The wt% of each component is measured on either side of the Matano plane, at t = 13 days after the start of the experiment are shown. (b) The corresponding profiles of the activity of carbon. Modeling and computational details are provided in Chapter 8 of the Supplementary Material.

between the force exerted per mole of species i with the drag, or friction, experienced with each of the partner species in the mixture. We may expect the frictional drag to be proportional to differences in the velocities of the diffusing species $(u_i - u_j)$. For a mixture containing a total of n components, 1, 2, 3,. . .n we write

$$-\frac{d\mu_i}{dz} = \sum_{j=1 j\neq i}^{n} \frac{RT}{Đ_{ij}} x_j (u_i - u_j); \quad i = 1, 2..n \tag{2}$$

The left member of Eq. (2) is the negative of the gradients of the chemical potential, with the units N mol^{-1}; it represents the driving force acting per mole of species i. The term $RT/Đ_{ij}$ is interpreted as the friction, or drag, coefficient for the i-j pairs. The multiplier x_j in each of the right members represents the mole fraction in the mixture because we expect the friction to be dependent on the number of molecules of j relative to that of component i. Other choices of composition measures, such as mass fractions, ω_i, and volume fractions, φ_i, are often used in describing diffusion in polymeric systems (Fornasiero et al., 2005; Heintz and Stephan, 1994; Krishna, 2016e, 2017b; Price and Romdhane, 2003; Ribeiro et al., 2011; Vrentas and Duda, 1979). The M–S diffusivity $Đ_{ij}$ has the units m^2 s^{-1} and the physical significance of an *inverse* drag coefficient. Chapter 9 of the Supplementary material provides a derivation of Eq. (2) from the fundamental principles of the thermodynamics of irreversible processes (Lightfoot, 1974). The Onsager reciprocal relations demand that the M–S pair diffusivities be symmetric $Đ_{ij} = Đ_{ji}$. The magnitudes of the M–S diffusivities $Đ_{ij}$ do not depend on the choice of the mixture reference velocity because Eq. (2) is set up in terms of velocity differences. Additional driving forces such as the electrostatic potential gradient, and pressure gradients can be added to the left members of Eq. (2), without alteration of the values of the drag coefficients for the i-j pairs.

The M–S Eqs. (2) serve as the appropriate starting point to the analysis and quantitative modeling of uphill diffusion in fluid mixtures, alloys, glasses, ionic systems, and microporous materials. The Supplementary Material accompanying this article provides more detailed derivations of the M–S equations, along with solu-

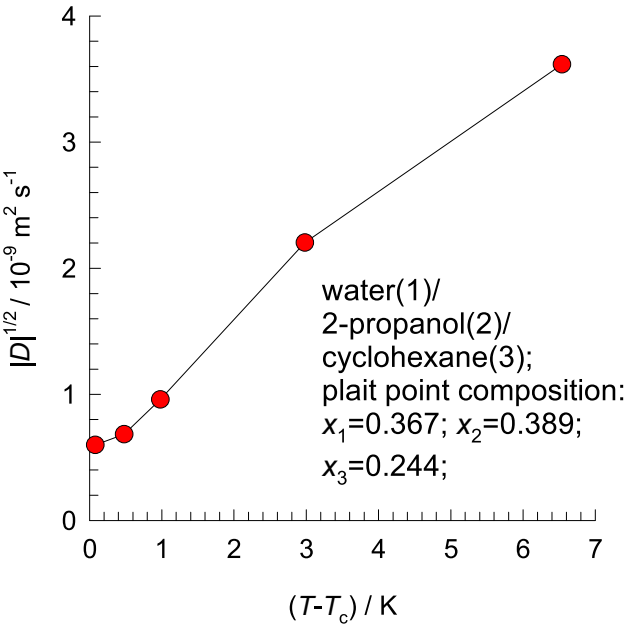

Fig. 8. Experimental data of (Clark and Rowley, 1986) for $|D|^{1/2}$ for water(1)/2-propanol(2)/cyclohexane(3) mixtures as function of $(T - T_c)$ where T is the temperature at which the diffusivities are measured, with T_c = 303.67 K. The elements of the Fick matrix of diffusivities were measured at a constant composition of the plait point at 303.67 K: x_1 = 0.367, x_2 = 0.389, x_3 = 0.244.

tions to the model equations describing transient equilibration in gaseous mixtures, multicomponent distillation, ternary liquid-liquid extraction, mixed electrolyte solutions, ion exchange processes, crystalline solids, alloys, silicates, and microporous materials. All the necessary data sources and inputs, procedures for estimation of diffusivities, and calculation methodologies are provided in the Supplementary Material; this should enable the interested reader to reproduce all the calculations and results presented and discussed in this review article.

2. Relating the M–S formulation to the generalized Fick's law

For n-component mixtures, the molar fluxes N_i in the laboratory fixed reference frame are defined as

$$N_i \equiv c_i u_i; \quad N_t = \sum_{i=1}^{n} N_i \tag{3}$$

The molar diffusion flux of species i, J_i, is defined with respect to the molar average reference velocity of the mixture, $u = x_1 u_1 + x_2 u_2 + \cdots x_n u_n$:

$$J_i \equiv c_i(u_i - u) = N_i - x_i N_t; \quad i = 1, 2, ..n \tag{4}$$

Multiplying both sides of Eq. (2) by $\frac{x_i}{RT}$, we obtain

$$-\frac{x_i}{RT}\frac{d\mu_i}{dz} = \sum_{\substack{j=1 \\ j\neq i}}^{n} \frac{x_j J_i - x_i J_j}{c_t Đ_{ij}} = \sum_{\substack{j=1 \\ j\neq i}}^{n} \frac{x_j N_i - x_i N_j}{c_t Đ_{ij}}; \qquad i = 1, 2, ..n \tag{5}$$

At constant temperature, T, and pressure, p, only $(n-1)$ of the chemical potential gradients are independent because of the Gibbs-Duhem constraint $\sum_{i=1}^{n} x_i \frac{d\mu_i}{dz} = 0$. The diffusion fluxes sum to zero $\sum_{i=1}^{n} J_i = 0$, and only $(n-1)$ of the molar diffusion fluxes are independent.

The chemical potential gradients are related to the mole fraction gradients by introducing a $(n-1)\,\mathrm{X}\,(n-1)$ dimensional matrix of thermodynamic factors $[\Gamma]$:

$$\frac{x_i}{RT}\frac{d\mu_i}{dz} = \sum_{j=1}^{n-1} \Gamma_{ij}\frac{dx_j}{dz}; \qquad \Gamma_{ij} = \delta_{ij} + x_i \frac{\partial \ln \gamma_i}{\partial x_j}; \qquad i, j = 1, 2, ..n-1 \tag{6}$$

The Γ_{ij} can be calculated from models describing phase equilibrium thermodynamics such as UNIQUAC, NRTL, Flory-Huggins, sub-regular solution models, or Redlich-Kister equations (Krishna, 2016e; Sandler, 1999; Taylor and Krishna, 1993). For dense gas mixtures, the thermodynamic correction factors can be determined using an appropriate equation of state (Krishna and

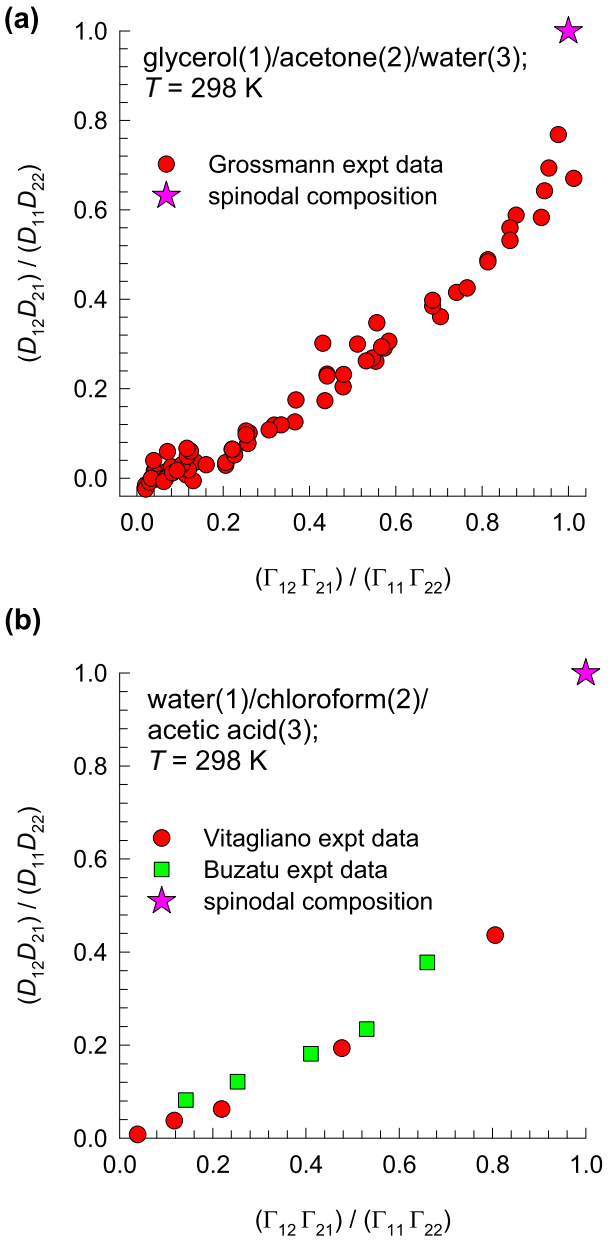

Fig. 9. (a, b) The ratio $\frac{D_{12}D_{21}}{D_{11}D_{22}}$ of the elements of the Fick diffusivity matrix $[D]$ plotted against the corresponding value of the ratio $\frac{\Gamma_{12}\Gamma_{21}}{\Gamma_{11}\Gamma_{22}}$ for (a) glycerol(1)/acetone(2)/water(3), and (b) water(1)/chloroform(2)/acetic-acid(3) mixtures. Calculation details are provided in Chapter 5 of the Supplementary material.

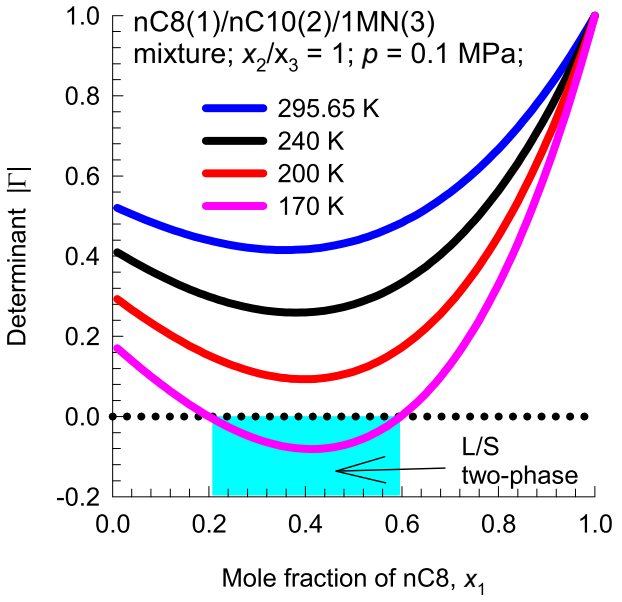

Fig. 10. Calculations using the Peng-Robinson equation of state, for the determinant $|\Gamma|$ for the ternary mixture of $nC_8H_{18}(1)/nC_{10}H_{22}(2)$/1-methylnapthalene(3) as a function of the composition of nC_8H_{18}, x_1, keeping the ratio x_2/x_3 at a constant value of unity. The calculations are presented for four different temperatures T = 295.65 K, 240 K, 200 K, and 170 K. The calculation details are provided by (Krishna and van Baten, 2016).

van Baten, 2016). In the special case of thermodynamically ideal mixtures, $[\Gamma]$ degenerates to yield $\Gamma_{ij} = \delta_{ij}$, where δ_{ij} is the Kronecker delta.

Using $(n-1)$ dimensional matrix notation, Eq. (5) may be recast into a form in which the $(n-1)$ independent diffusion fluxes are explicitly related to the $(n-1)$ independent mole fraction gradients

$$(J) = -c_t[D]\frac{d(x)}{dz} \tag{7}$$

Eq. (7) defines the $(n-1)\times(n-1)$ dimensional matrix of Fick diffusivities $[D]$, that relates the $(n-1)$ dimensional column matrix of fluxes (J), to the $(n-1)$ dimensional column matrix of mole fraction gradients $\frac{d(x)}{dz}$; this relation may be regarded as the proper generalization of Eq. (1) for n-component mixtures. Combination of Eqs. (5), (6), and (7) allows us to derive the following explicit expression for the matrix of Fick diffusivities $[D]$ as a product of two matrices

$$[D] = [\Lambda][\Gamma]; \quad [\Lambda] = [B]^{-1} \tag{8}$$

In Eq. (8), the elements of the $(n-1)\times(n-1)$ dimensional matrix $[B]$ are given by

$$B_{ii} = \frac{x_i}{Đ_{in}} + \sum_{\substack{k=1\\k\neq i}}^{n}\frac{x_k}{Đ_{ik}}; \quad B_{ij(i\neq j)} = -x_i\left(\frac{1}{Đ_{ij}} - \frac{1}{Đ_{in}}\right); \quad i,j = 1,2\ldots n-1 \tag{9}$$

For a ternary mixture, n = 3, Eqs. (8), and (9) yield the following explicit expression for $[\Lambda]$ in terms of the M–S diffusivities of the constituent binary pairs in the ternary mixture (Krishna, 2015b)

$$\begin{bmatrix}\Lambda_{11} & \Lambda_{12}\\ \Lambda_{21} & \Lambda_{22}\end{bmatrix} = \frac{\begin{bmatrix} Đ_{13}(x_1Đ_{23} + (1-x_1)Đ_{12}) & x_1Đ_{23}(Đ_{13} - Đ_{12})\\ x_2Đ_{13}(Đ_{23} - Đ_{12}) & Đ_{23}(x_2Đ_{13} + (1-x_2)Đ_{12})\end{bmatrix}}{x_1Đ_{23} + x_2Đ_{13} + x_3Đ_{12}} \tag{10}$$

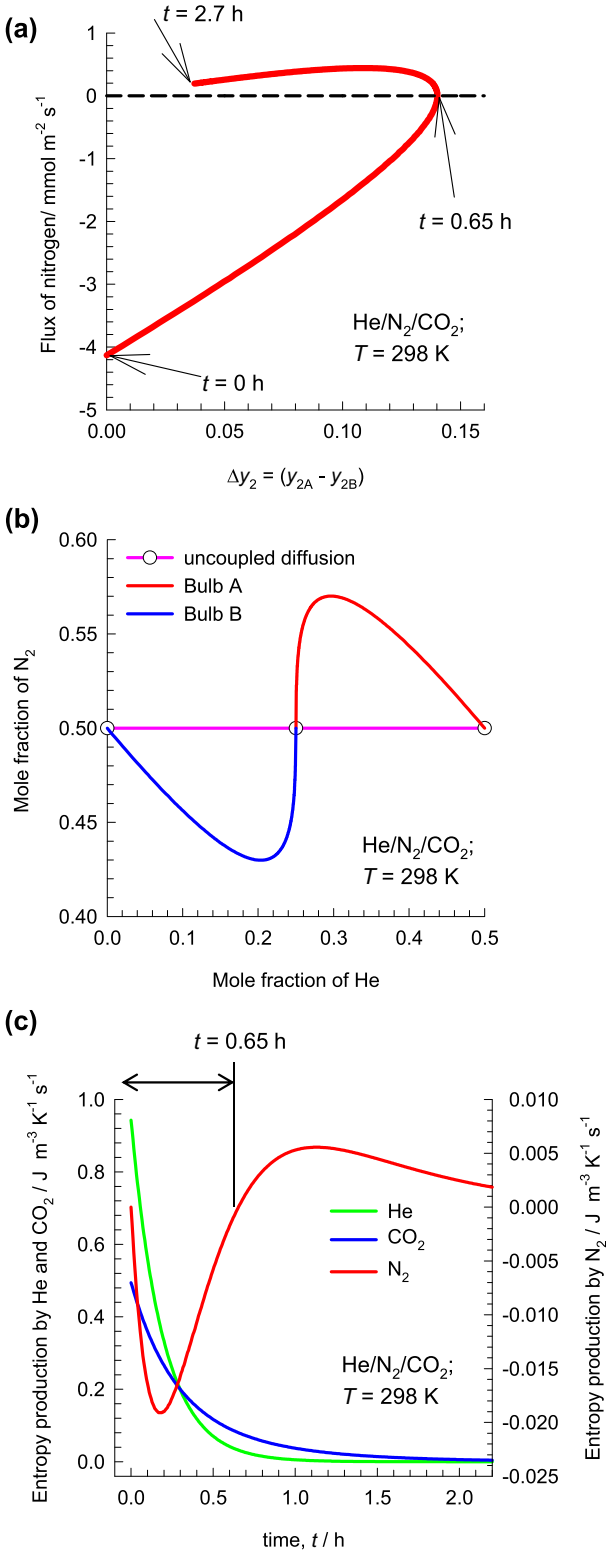

Fig. 11. Analysis of the transient approach to equilibrium in the two-bulb diffusion experiments for He(1)/N_2(2)/CO_2(3) mixtures. (a) Plot of the instantaneous flux of nitrogen (species 2) versus the difference in the mole fractions of nitrogen in bulbs A and B. (b) Equilibration trajectories in the two bulbs plotted in composition space. (c) Calculations of the individual rates of entropy production of the three species as a function of time. Modeling and computational details are provided in Chapter 3 of the Supplementary Material.

Eqs. (8), (9), and (10) shows that two kinds of "coupling" may contribute to off-diagonal contributions of the Fickian matrix [D]: (a) differences in the M–S diffusivities of the binary pairs, $Đ_{ij}$, and (b) thermodynamic coupling, quantified by the off-diagonal elements of [Γ].

3. Influence of thermodynamic corrections on [D]

Experimental data for a wide variety of ternary liquid mixtures (Alimadadian and Colver, 1976; Buzatu et al., 2007; Cullinan and Toor, 1965; Grossmann and Winkelmann, 2005, 2007a, 2007b; Rehfeldt and Stichlmair, 2010; Shuck and Toor, 1963; Vitagliano et al., 1978) confirm that the off-diagonal elements of the Fick matrix [D] are generally non-zero, and their magnitudes are strongly influenced by the thermodynamic correction factors Γ_{ij}. In order to underscore the influence of Γ_{ij} on the elements of the the Fickian matrix [D], we consider diffusivities in glycerol(1)/acetone(2)/water(3) mixtures that exhibit partial miscibility; see Fig. 2. Outside the region delineated by the binodal curve, we have the requirement that needs to be fulfilled for phase stability in homogeneous liquid mixtures (detailed discussions are available in Chapter 5 of the Supplementary Material)

$$|\Gamma| > 0; \quad \text{phase stability} \tag{11}$$

Within the region delineated by the spinodal curve, there is the region of phase instability

$$|\Gamma| < 0; \quad |D| < 0; \quad \text{phase instability} \tag{12}$$

Eq. (12) implies that one of eigenvalues of the Fick diffusivity matrix [D] must be negative. At the plait point, the binodal and spinodal curves converge; the region between the binodal and spinodal curves is *meta*-stable. Along the spinodal curve we have (Vitagliano et al., 1978)

$$|\Gamma| = 0; \quad |D| = 0; \quad \text{spinodal curve} \tag{13}$$

(Clark and Rowley, 1986) report experimental data for $|D|$ in water(1)/2-propanol(2)/cyclohexane(3) mixtures, measured at constant compositions corresponding to the plait point, and varying temperatures, T. In accordance with Eq. (13), the magnitude

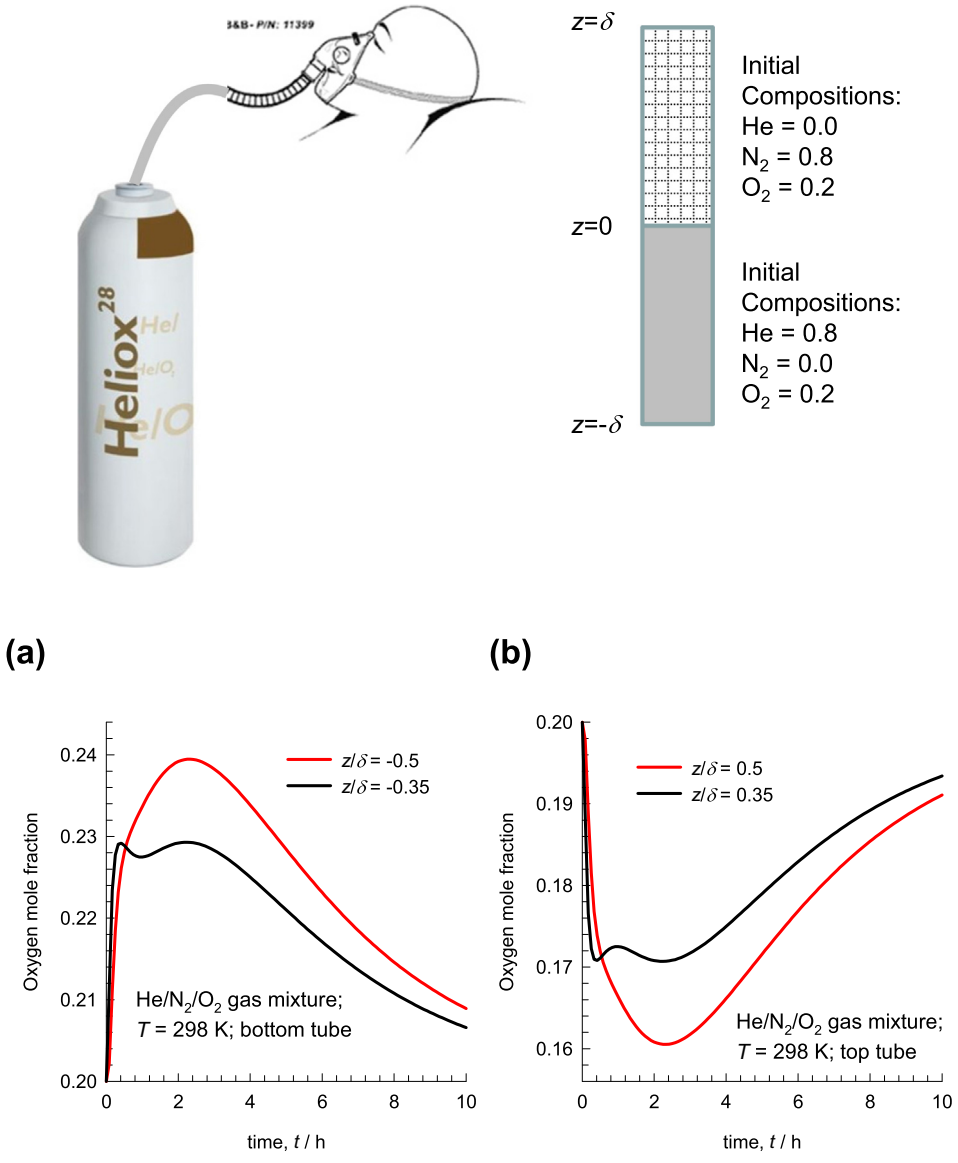

Fig. 12. Heliox therapy modeled as inter-diffusion of He(1)/N_2(2)/O_2(3) mixtures between two cylindrical Loschmidt tubes. (a, b) The transient equilibration trajectories O_2 in the (a) top, and (b) bottom compartments at the positions $z/\delta = \pm 0.35$, and $z/\delta = \pm 0.5$. Modeling and computational details are provided in Chapter 3 of the Supplementary Material.

of $|D|^{1/2}$ decreases progressively as T approaches the critical temperature $T_c = 303.67$ K, corresponding to phase transition; see Fig. 8.

Eq. (13) also implies that for any partially miscible ternary mixture, thermodynamic coupling effects become of paramount importance in the regions close to phase splitting. As verification, we examine four experimental data sets on the Fick diffusivity matrix [D] for glycerol(1)/acetone(2)/water(3) mixtures, all measured at a constant glycerol mole fraction, $x_1 = 0.1$; see Fig. 2. At composition E, the experimental data on the elements of the Fick diffusivity are $[D] = \begin{bmatrix} 0.3868 & 0.0184 \\ 0.1477 & 0.407 \end{bmatrix} \times 10^{-9}$ m^2 s^{-1}. The importance of diffusional coupling may be quantified by the ratio $\frac{D_{12}D_{21}}{D_{11}D_{22}} = 0.01725$. The magnitude of diffusional coupling progressively increases as the compositions approaches the spinodal curve, along which Eq. (13) must be satisfied. Fig. 9a presents a plot of the ratio $\frac{D_{12}D_{21}}{D_{11}D_{22}}$ of the elements of the Fick diffusivity matrix [D] as a function of the ratio $\frac{\Gamma_{12}\Gamma_{21}}{\Gamma_{11}\Gamma_{22}}$ for the entire data set for 75 different compositions reported by (Grossmann and Winkelmann, 2005, 2007a, 2007b); we see a unique dependence between the two sets of data. Fig. 9b presents an analogous plot for water(1)/chloroform (2)/acetic-acid(3) mixtures using the experimental data reported by (Vitagliano et al., 1978) and (Buzatu et al., 2007). The important conclusion to be drawn from the plots in Fig. 9a,b is that the off-diagonal elements of the Fick diffusivity matrix have their origins in thermodynamic influences.

By detailed and careful examination of large sets of experimental data on Fick matrix [D] for ternary liquid mixtures (Krishna, 2015b, 2016b), it has been established that coupling effects in the Fick matrix emanate predominantly from [Γ]. Indeed, a reasonably accurate for estimation of the elements of [D] for ternary mixtures is

$$[D] = |\Lambda|^{1/2}[\Gamma] \tag{14}$$

in which the square-root of the determinant of [Λ]:

$$|\Lambda|^{1/2} = \sqrt{\frac{Đ_{12}Đ_{13}Đ_{23}}{x_1Đ_{23} + x_2Đ_{13} + x_3Đ_{12}}} \tag{15}$$

provides an appropriate measure of the scalar magnitude of [Λ]; experimental validation of the accuracy of Eq. (14) is provided by (Krishna, 2015b, 2016b).

For estimation of the M–S binary pair diffusivities $Đ_{ij}$ in Eq. (15), the Vignes interpolation formula for binary liquid mixtures (Vignes, 1966) can be extended to ternary mixtures as follows (Krishna and van Baten, 2005)

$$Đ_{ij} = \left(Đ_{ij}^{x_i\to 1}\right)^{x_i}\left(Đ_{ij}^{x_j\to 1}\right)^{x_j}\left(Đ_{ij}^{x_k\to 1}\right)^{x_k} \tag{16}$$

The six infinite dilution values of the pair diffusivities $Đ_{ij}^{x_j\to 1}$ can be estimated using say the Wilke-Chang correlation (Reid et al., 1986). For estimation of $Đ_{ij}^{x_k\to 1}$, the i - j pair diffusivity when both i and j are present in infinitely dilute concentrations, the following formula has been suggested (Krishna and van Baten, 2005):

$$Đ_{ij}^{x_k\to 1} = \left(Đ_{ik}^{x_k\to 1}\right)^{x_i/(x_i+x_j)}\left(Đ_{jk}^{x_k\to 1}\right)^{x_j/(x_i+x_j)} \tag{17}$$

Strong thermodynamic coupling effects also manifest in composition regions close to liquid/solid phase transitions, of importance in crystallization and precipitation processes. For example, the melting points of nC_8H_{18}, $nC_{10}H_{22}$, and 1-methylnapthalene (1MN) are 216 K, 243 K, and 251 K, respectively. On cooling nC_8H_{18}(1)/$nC_{10}H_{22}$(2)/1-MN(3) mixtures, crystals of 1MN will be first to come out of solution and the 1MN can be separated from

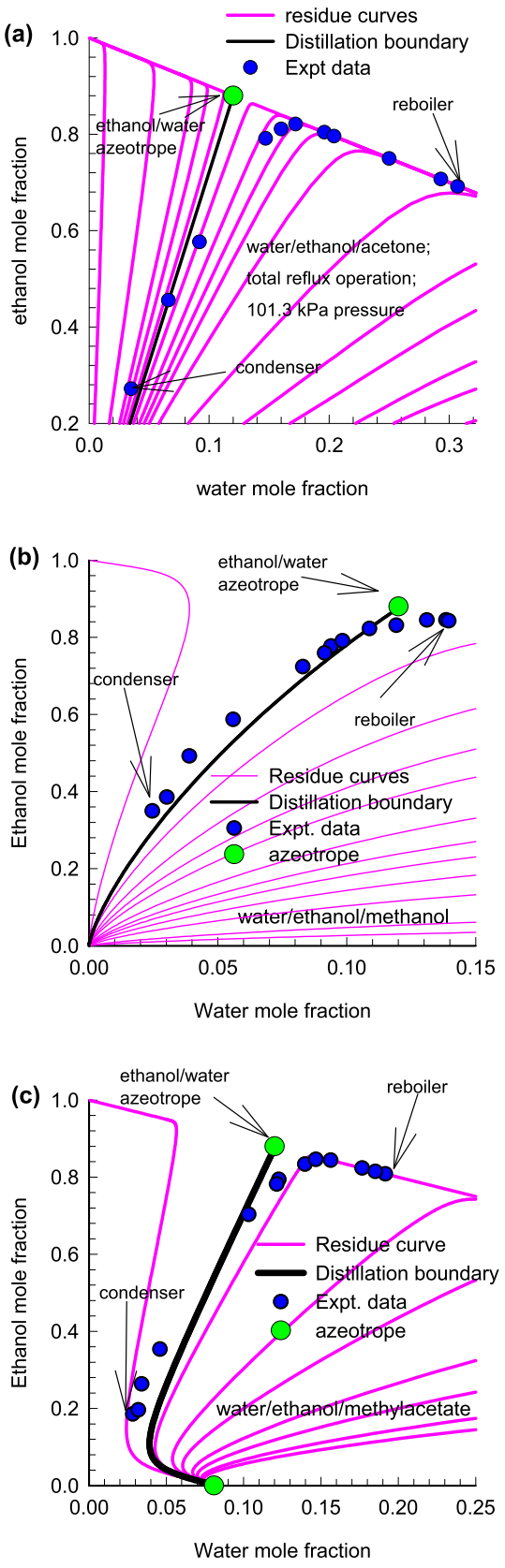

Fig. 13. Residue curve maps for distillation of (a) water/ethanol/acetone, (b) water/ethanol/methanol, and (c) water/ethanol/methyl-acetate mixtures. The symbols represent the experimental data of (Springer et al., 2002a,b,c,d) for composition trajectories in a bubble-cap tray column operating at total reflux implying $x_i = y_i$. Modeling and computational details are provided Chapter 4 of the Supplementary Material.

linear alkanes by fractional crystallization. Fig. 10 presents calculations for the determinant $|\Gamma|$ for $nC_8H_{18}/nC_{10}H_{22}$/1-MN mixtures as a function of the mole fraction of nC_8H_{18}, x_1, and T = 295.65 K, 240 K, 200 K, and 170 K. We note that at the lowest temperature, T = 170 K, there is a range of compositions for which $|\Gamma| < 0$, indicating phase instability and crystal formation. At T = 295.65 K and a liquid mixture composition $x_1 = 0.384$, $x_2 = 0.308$, $x_3 = 0.308$, we can evaluate the matrix of thermodynamic factors, $[\Gamma] = \begin{bmatrix} 0.486 & -0.305 \\ -0.068 & 0.9 \end{bmatrix}$. Multiplying $[\Gamma]$ by the estimated value $|\Lambda|^{1/2} = 3.4 \times 10^{-9}$ m^2 s^{-1}, yields $[D] = \begin{bmatrix} 1.65 & -1.03 \\ -0.23 & 3.06 \end{bmatrix} \times 10^{-9}$ m^2 s^{-1}. This estimated value is close to the experimentally determined value $[D] = \begin{bmatrix} 1.92 & -1.07 \\ -0.333 & 2.47 \end{bmatrix} \times 10^{-9}$ m^2 s^{-1} reported by (Leahy-Dios et al., 2005); see (Krishna and van Baten, 2016) for further details.

4. Uphill diffusion in ideal gas mixtures

For ideal gas mixtures, Eq. (5) simplifies to

$$-\frac{dy_i}{dz} = \sum_{\substack{j=1 \\ j\neq i}}^{n} \frac{y_j N_i - y_i N_j}{c_t Đ_{ij}} = \sum_{\substack{j=1 \\ j\neq i}}^{n} \frac{y_j J_i - y_i J_j}{c_t Đ_{ij}}; \qquad i = 1, 2, \ldots n \tag{18}$$

The M–S pair diffusivities $Đ_{ij}$ for gaseous mixtures at low pressures, below about 10 bar, can be estimated to a good level of accuracy using the (Fuller et al., 1966) method.

$$Đ_{12} = \frac{1.43 \times 10^{-7} T^{1.75}}{p_t \sqrt{M_{12}} \left[\left(v_1^{1/3} \right) + \left(v_2^{1/3} \right) \right]^2} \quad \text{m}^2\text{s}^{-1} \tag{19}$$

where p_t is the pressure (expressed in bars), $M_{12} = \frac{2}{\frac{1}{M_1} + \frac{1}{M_2}}$ is the mean molecular weight of the mixture (expressed in g mol^{-1}), v_1, and v_2

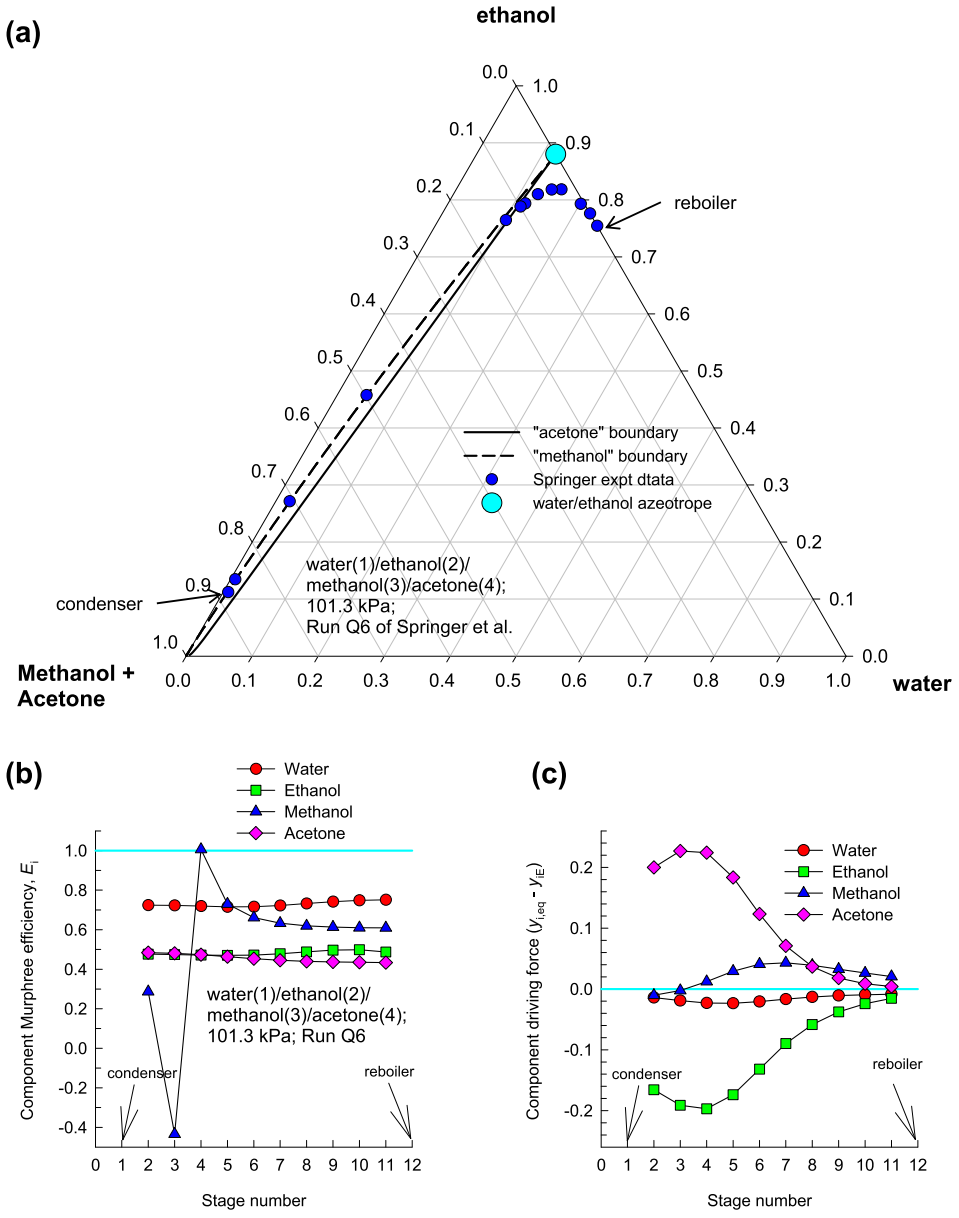

Fig. 14. (a) Experimental data (symbols) of (Springer et al., 2002c) for Run Q6 with quaternary water(1)/ethanol(2)/methanol(3)/acetone(4) mixtures in a 12-tray distillation column operating at total reflux. (b) Component Murphree efficiencies on each stage. (c) Component driving forces on each stage. Modeling and computational details are provided in Chapter 4 of the Supplementary Material.

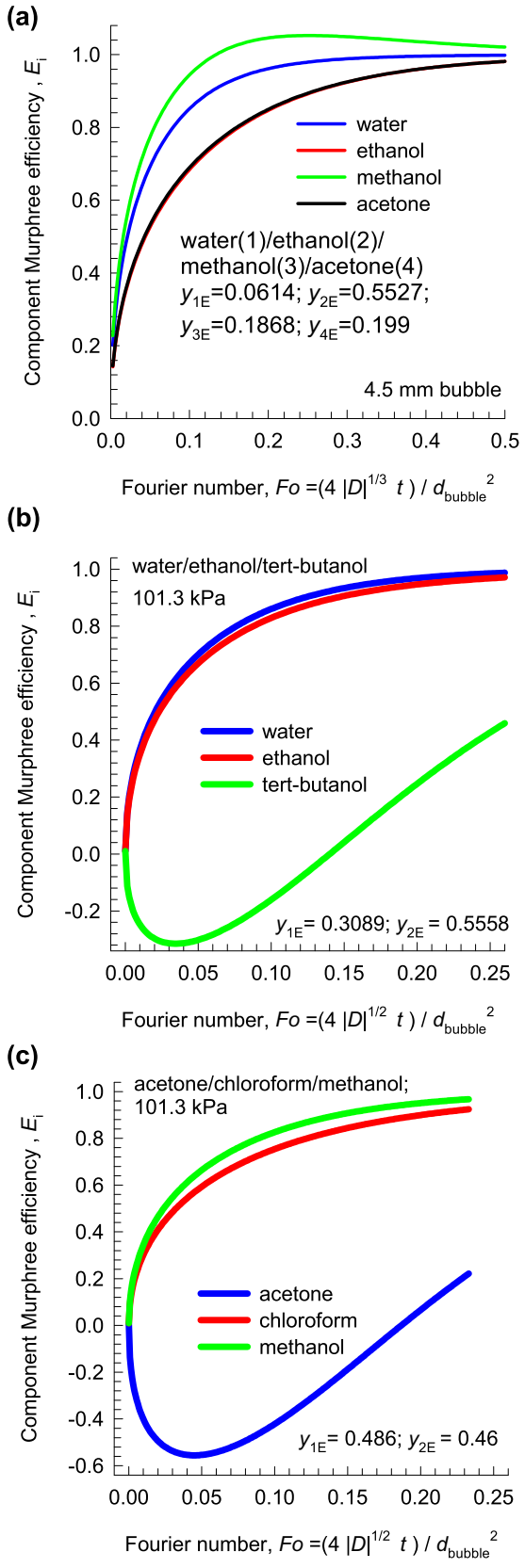

Fig. 15. Plot of the component Murphree efficiencies, E_i, as function of the Fourier number for (a) water(1)/ethanol(2)/methanol(3)/acetone(4), (b) water(1)/ethanol (2)/tert-butanol(3), and (c) acetone(1)/chloroform(2)/methanol(3) mixtures. Modeling and computational details are provided in Chapter 4 of the Supplementary Material.

are the diffusion volumes (expressed in cm^3 mol^{-1}) whose values are obtained by summing the contributions of the volumes of the constituent atoms in the molecular species (the values are tabulated in (Reid et al., 1986)). According to the FSG estimation procedure, the product of $Đ_{12}$ and the total pressure, p_t, is a function only of temperature and is also independent of composition.

The continuous solid lines in Fig. 1a–c represent the solutions to Eq. (18) along with the continuity equations; all computational details are provided in the Supplementary material accompanying this publication. The M–S equations quantitatively capture the transient overshoots/undershoot phenomena that signal occurrence of uphill diffusion. For elucidation of the phenomena of uphill diffusion, we examine the transient equilibration of He(1)/N_2(2)/CO_2(3) mixtures in the two bulb diffusion apparatus in which equimolar diffusion prevails: $N_t = 0$; $N_i = J_i$. The M–S pair diffusivities at p_t = 40 kPa, and T = 298 K, corresponding to the experiments in Fig. 1a, are estimated using Eq. (19) as $Đ_{12} = 17.8 \times 10^{-5}; Đ_{13} = 14.7 \times 10^{-5}; Đ_{23} = 4.1 \times 10^{-5}$ m^2 s^{-1}. Since $\Gamma_{ij} = \delta_{ij}$ for ideal gas mixtures, the Fick diffusivity matrix $[D] = [\Lambda]$ can be calculated using Eq. (10). The compositions in the two bulbs equilibrate after several hours to $y_{1,eq}$ = 0.25, $y_{2,eq}$ = 0.5 and $y_{3,eq}$ = 0.25. At this equilibrium composition the elements of the Fick diffusivity matrix $[D] = \begin{bmatrix} 16.45 & -0.25 \\ -7.83 & 5.2 \end{bmatrix} \times 10^{-5}$ m^2 s^{-1}. The large negative value of the off-diagonal D_{21} causes the flux of nitrogen (species 2) to be strongly coupled to the driving force of He (component 1).

Fig. 11a presents a plot of the instantaneous flux of nitrogen (species 2) versus the difference in the mole fractions of nitrogen in bulbs A and B, $\Delta y_2 = y_{2A} - y_{2B}$. At time t = 0, there is no driving force of species 2 (nitrogen), $\Delta y_2 = 0$, but the nitrogen flux is non-zero because of the non-zero contribution of $\frac{c_t}{\delta} D_{21}(y_{1A}(t=0) - y_{1B}(t=0))$; the flux of nitrogen has a large negative value of -4.1 mmol m^{-2} s^{-1}. During the time interval $0 < t < 0.65$ h, the flux of nitrogen is negative, i.e. directed from bulb B to bulb A, despite the fact that $\Delta y_2 = y_{2A} - y_{2B} > 0$; in other words, nitrogen diffuses in a direction opposite to that dictated by its own driving force; the root cause of uphill transport can be traced to the negative contribution of $\frac{c_t}{\delta} D_{21} \Delta y_1$. Only for $t > 0.65$ h, does nitrogen diffuse down its own composition gradient. The transient equilibration process in Bulbs A and B follow serpentine trajectories when plotted in composition space; see Fig. 11b. If the M–S diffusivities of all the binary pairs in the mixture are close to each other in value, i.e. $Đ_{12} \approx Đ_{13} \approx Đ_{23} \approx Đ$, Eq. (7) degenerate to yield $J_i = -c_t Đ \frac{dy_i}{dz}$; in this degenerate scenario the flux of any component is proportional to its own composition gradient; the transient equilibration process follows a linear trajectory and there is no uphill diffusion of nitrogen.

The occurrence of uphill diffusion is not in violation of the second law of thermodynamics; the second law requires that the total rate of entropy produced by all diffusing species should be positive definite (Kuiken, 1994; Standart et al., 1979):

$$\sigma = -\frac{1}{T} \sum_{i=1}^{n} \frac{d\mu_i}{dz} J_i \tag{20}$$

For equimolar diffusion of ideal ternary gas mixtures, Eq. (20) simplifies to

$$\sigma = -R \left[J_1 \frac{1}{y_1} \frac{dy_1}{dz} + J_2 \frac{1}{y_2} \frac{dy_2}{dz} + J_3 \frac{1}{y_3} \frac{dy_3}{dz} \right] \geqslant 0 \tag{21}$$

The individual rates of entropy production of the three constituent species are plotted in Fig. 11c. We note that the rate of entropy production by nitrogen (species 2) is negative during the

time interval $0 < t < 0.65$ h. However, the second law of thermodynamics is not violated because the other two species, helium and carbon dioxide produce entropy at significantly higher rates, ensuring that $\sigma \geqslant 0$ is satisfied during the entire equilibration process.

5. Uphill diffusion of O_2 in heliox therapy

While the data in Fig. 1 provide a theoretical justification of the need for adopting the M–S formulation for calculation of fluxes, it is less well appreciated that the phenomena of uphill diffusion is important in treatment of patients with respiratory problems. In diffusion processes in lung airways, normally four gases are involved: O_2, CO_2, N_2, and H_2O; the Maxwell-Stefan Eq. (5) are commonly used to model pulmonary gas transport (Boudin et al., 2010; Bres and Hatzfeld, 1977; Chang and Farhi, 1973; Chang et al., 1975; Jebria, 1987; Jebria and Bres, 1982; Tai, 1979). The transport of the fresh breathed-in air towards the acini of human beings with chronic obstructive bronchopneumopathy, such as asthma, is rendered difficult due to bronchoconstriction and other factors (Boudin et al., 2010; Chevrolet, 2001; Chiappa et al., 2009). Such patients need some respiratory support to allow the oxygen to be transported through the proximal bronchial tree and then diffused in the distal one. One such support system consists of the inhalation of a mixture of heliox (20% O_2; 80% He), that facilitates the transport of oxygen, and exhalation of CO_2.

We model the ternary He(1)/N_2(2)/O_2(3) mixture diffusion process as inter-diffusion between two cylindrical Loschmidt tubes each of length δ as pictured in Fig. 12. Fig. 12a,b shows the transient equilibration of O_2 in the (a) top, and (b) bottom compartments at the positions $z/\delta = \pm 0.35$, and $z/\delta = \pm 0.5$, calculated using the M–S Eq. (5), along with the continuity relations (Arnold and Toor, 1967; Ravi, 2007; Taylor and Krishna, 1993). The overshoot of O_2 composition in the bottom compartment signals uphill diffusion; this overshoot has been verified in the experimental data of (Bres and Hatzfeld, 1977). The corresponding transient equilibration of O_2 in the top compartment tube displays undershoots. If coupling effects are ignored entirely, no oxygen transport in feasible.

Simulations using different inert gases such as argon and sulfur hexafluoride in place of helium show that no uphill transport of

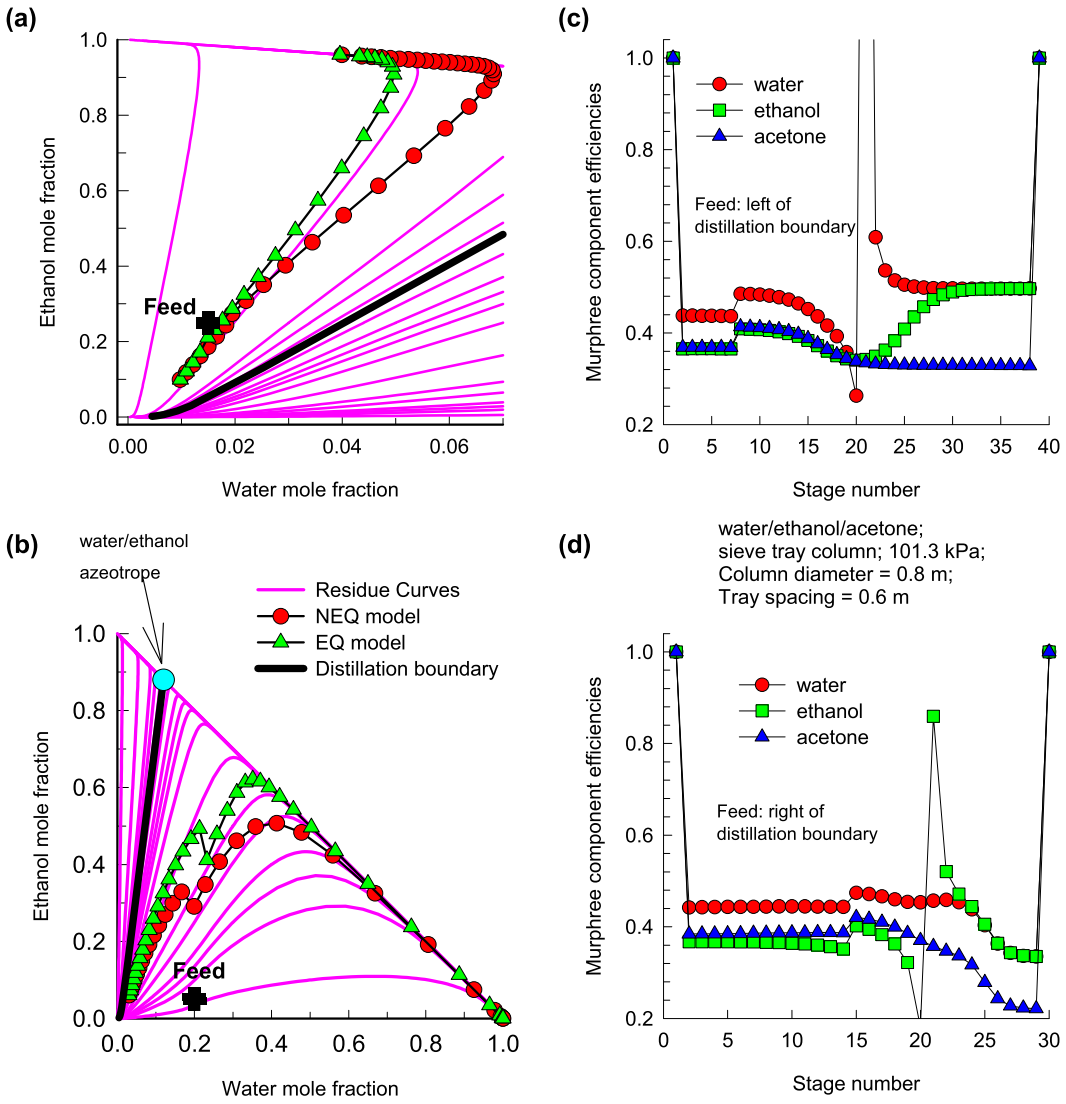

Fig. 16. Comparison of column composition trajectories calculated using the NEQ with EQ stage model for distillation of water/ethanol/acetone feed mixtures in a sieve-tray column of 0.8 m diameter, operating at a total pressure of 101.3 kPa. (a) Feed composition is to the left of the distillation boundary. (b) Feed composition is to the right of the distillation boundary. (c, d) Component Murphree efficiencies calculated using the NEQ model. Modeling and computational details are provided in the Supplementary material accompanying (Krishna, 2016b).

oxygen occurs because the binary pair diffusivities are close to one another; see Chapter 3 of Supplementary material. Put another way, the efficacy of heliox therapy relies on uphill transfer of oxygen.

6. Murphree efficiencies in multicomponent distillation

Residue curve maps (RCM) are widely used for examining feasible separation schemes for distillation of mixtures that form homogeneous or heterogeneous azeotropes (De Villiers et al., 2002; Doherty and Malone, 2001; Wankat, 2012). RCMs describe the change of the composition of the liquid phase during continuous evaporation under conditions in which vapor–liquid equilibrium is maintained, and serve as "tramlines" for column composition trajectories in a distillation tower. As illustration, Fig. 13 shows the RCMs for (a) water(1)/ethanol(2)/acetone(3), (b) water/ethanol/methanol, and (c) water/ethanol/methylacetate mixtures at 101.3 kPa. For each of these mixtures, the solid black line with the ethanol/water azeotrope at one end, divides the ternary composition space into two distinct regions. As argued by (Levy et al., 1985) the column composition trajectories calculated by an equilibrium (EQ) stage model cannot cross the boundaries in Fig. 13a–c.

The symbols in Fig. 13a–c represent the experimental data for composition trajectories in a 12-tray bubble-cap column operating at total reflux implying $x_i = y_i$. For all three mixtures, the condenser composition is to the left of the distillation boundary, and the reboiler composition (richer in water) is towards the right of the distillation boundary. In other words, the distillation boundary is crossed in all three sets of experiments, despite the fact that such crossing is infeasible if the EQ stage model is used. Detailed examination of interphase mass transfer processes, using the M–S equations (Krishna, 2016b) for transfer in both vapor and liquid phases, show that the boundary crossing phenomena is engendered by unequal component Murphree efficiencies (Murphree, 1925) defined by

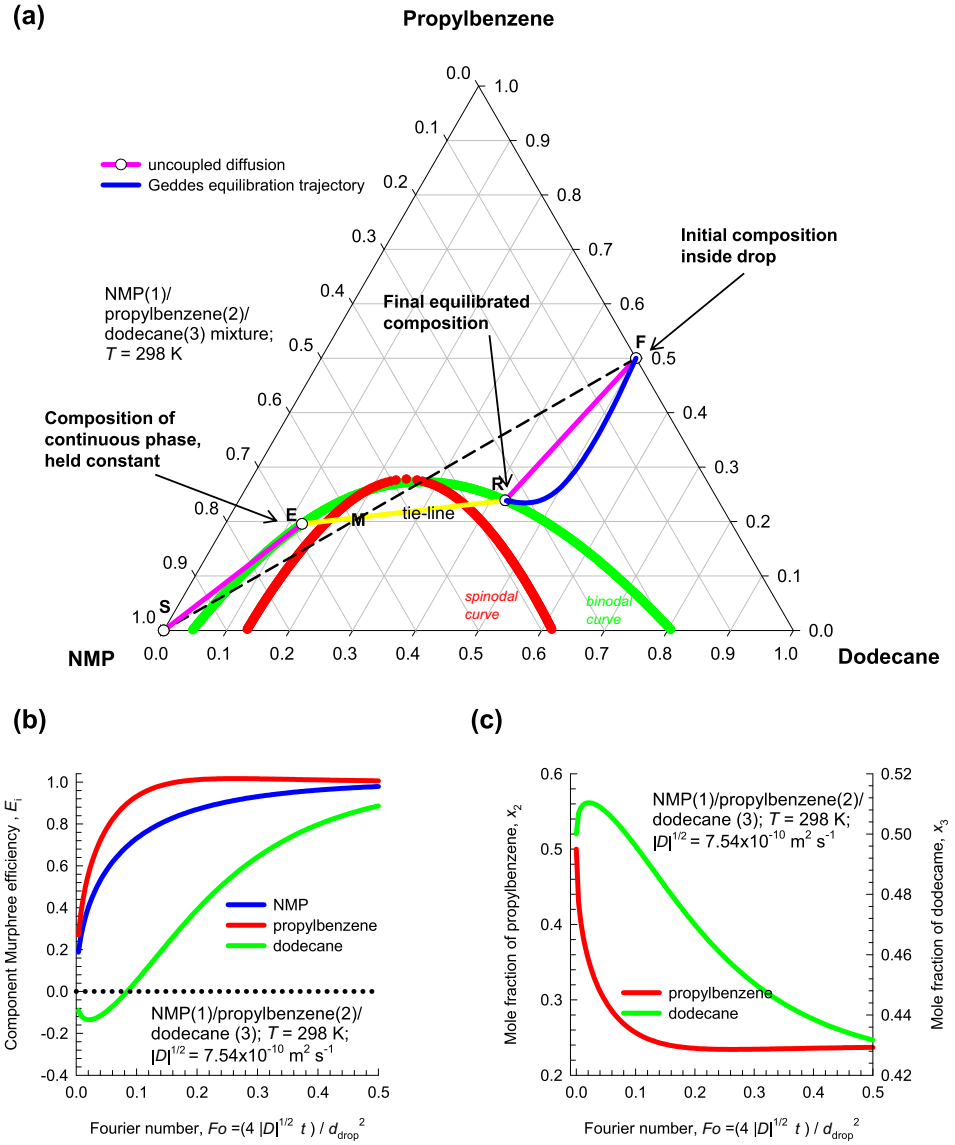

Fig. 17. (a) The phase equilibrium diagram for the system NMP(1)/propylbenzene(2)/dodecane(3) at 298 K. Pure N-methyl pyrrolidone (NMP, S = solvent) is mixed with a 50/50 propylbenzene/dodecane feed mixture (F) to yield mixture M that lies in the two phase region. The plait point is indicated by P. The mixture separates into two phases with compositions E (Extract) and R (Raffinate) at either ends of the tie-line shown. The feed phase F will equilibrate to R, and the solvent phase S will equilibrate to E. (b) Plot of the component Murphree efficiencies, E_i, as function of the Fourier number. (c) Plot of the transient equilibration compositions of propylbenzene and dodecane as a function of the Fourier number. Modeling and computational details are provided in Chaper 6 of the Supplementary Material.

$$E_i = \frac{y_{i0} - y_i}{y_{i0} - y_{ieq}} \tag{22}$$

where y_{i0}, and y_i are, respectively, the vapor phase mole fractions, entering and leaving a tray, and y_{ieq} is the vapor composition in thermodynamic equilibrium with the liquid leaving the tray. For binary distillation, the Murphree component efficiencies are bounded, i.e. $0 \leqslant E_1 = E_2 \leqslant 1$. For multicomponent distillation, with the number of species $n \geqslant 3$, coupled diffusion effects in either vapor or liquid phases cause the component efficiencies to be distinctly different from one another, $E_1 \neq E_2 \neq E_3 \ldots \neq E_n$; see Chapter 4 of Supplementary material. If uphill diffusion manifests, the component efficiencies may be unbounded, with values less than zero, $E_i < 0$, or exceeding unity, $E_i > 1$; such occurrences are explored and analyzed hereunder.

Fig. 14a presents the experimental data of (Springer et al., 2002c) for distillation of the quaternary water(1)/ethanol(2)/methanol(3)/acetone(4) mixture in a 12-stage distillation column. The ethanol/water azeotrope essentially divides the composition space into distinct regions, separated by two distillation boundaries connecting the ethanol/water azeotrope to the methanol, and acetone vertices; the experimentally determined column composition profile crosses both these boundaries. The experimentally determined component Murphree efficiency of methanol is negative on stage 3, $E_3 < 0$, and slightly exceeds unity on stage 4, $E_3 > 1$; see Fig. 14b. This implies that uphill diffusion of methanol manifests on both stages 3 and 4. The rationalization is to be found in the fact that the driving force of methanol is practically zero on these two stages (see Fig. 14c); the direction of transport of methanol is dictated by the transfer of the three partner species in the mixture: water, ethanol, and acetone. Methanol is "dragged" uphill due to because of the larger fluxes of the partner species in the mixture.

For modeling uphill diffusion of methanol, the transient equilibration process inside a spherical vapor bubble, of diameter d, dispersed in a liquid on a tray is described by the (Geddes, 1946) model. For n-component mixtures, the Geddes model can be written in $(n-1)$ dimensional matrix notation (Krishna, 1985; Taylor and Krishna, 1993)

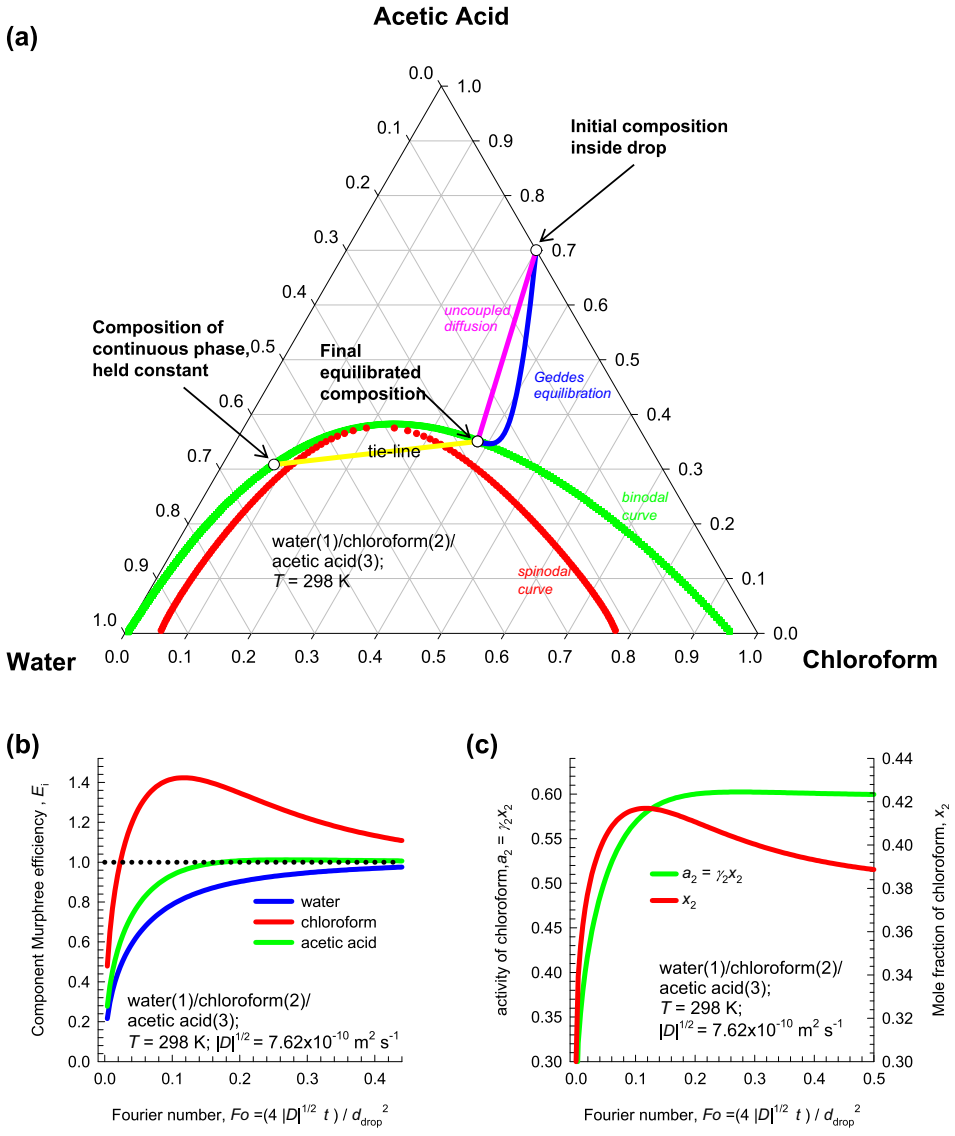

Fig. 18. (a) Transient equilibration trajectories for water(1)/chloroform(2)/acetic-acid(3) mixture, calculated using the Geddes model, plotted in composition space. The initial mole fractions of the dispersed phase droplet is $x_{10} = 0.0$, $x_{20} = 0.3$, and $x_{30} = 0.7$. (b) Plot of the component Murphree efficiencies, E_i, as function of the Fourier number. (c) Plot of the transient equilibration mole fractions and activities of chloroform as a function of the Fourier number. Modeling and computational details are provided in Chapter 6 of the Supplementary Material.

$$(y - y_{eq}) = [Q](y_0 - y_{eq}); \quad [Q] \equiv \frac{6}{\pi^2}\sum_{m=1}^{\infty}\frac{1}{m^2}\exp\left[-m^2\pi^2\frac{4[D]t}{d^2}\right] \tag{23}$$

The matrix [Q] quantifies the departure from equilibrium. The matrix of Fick diffusivities in the vapor bubble is estimated as

$$\begin{bmatrix} D_{11} & D_{12} & D_{13} \\ D_{21} & D_{22} & D_{23} \\ D_{31} & D_{32} & D_{33} \end{bmatrix} = \begin{bmatrix} 2.08543 & -0.00713 & -0.02297 \\ -0.55018 & 1.00661 & -0.20879 \\ -0.23304 & -0.02717 & 1.30245 \end{bmatrix} \times 10^{-5}$$

$m^2\ s^{-1}$; for calculation details see Chapter 4 of Supplementary material. Not all of the off-diagonal elements of [D] are negligibly small, and coupling effects are of significant importance. For conditions representative of stage 4 in the Springer experiments (cf. Fig. 14a), the component Murphree efficiencies are plotted in Fig. 15a, as a function of the Fourier number. The hierarchy of component efficiencies is $E_3 > E_1 > E_2 \approx E_4$, identical to the one determined experimentally (cf. Fig. 14b). The Geddes model correctly anticipates uphill diffusion of methanol, causing $E_3 > 1$,

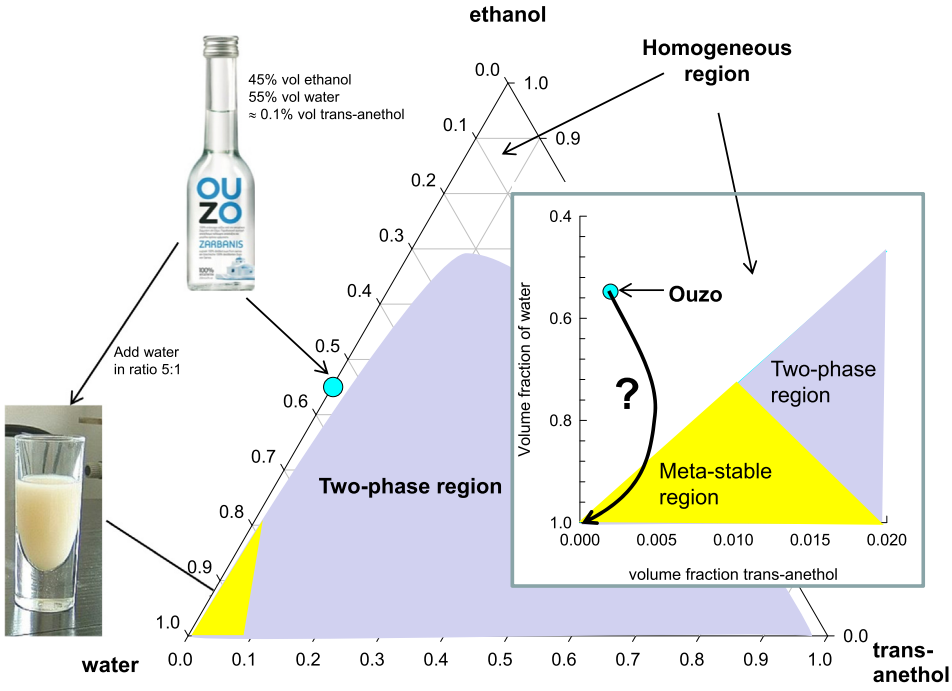

Fig. 19. Phase equilibrium diagram for the ternary mixture of trans-anethol/ethanol/water (Sitnikova et al., 2005). Also shown is the typical composition of Ouzo that is three component mixture of ethanol (≈45 vol%), water (55 vol%) and an essential oil called trans-anethol (≈0.1%).

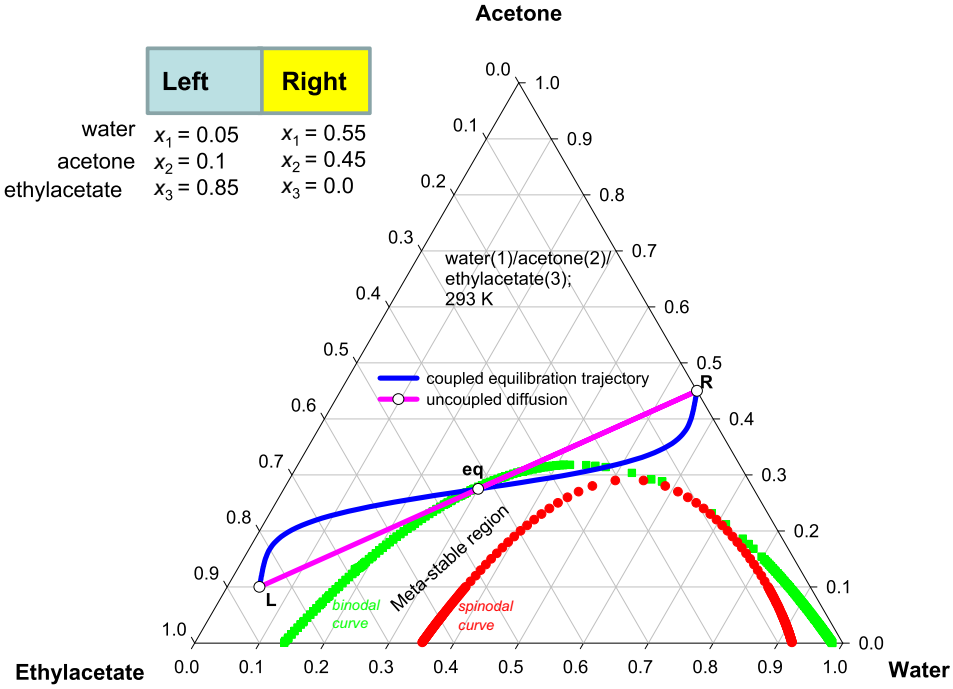

Fig. 20. Trajectory followed during equilibration of homogenous mixtures of two different compositions for water(1)/acetone(2)/ethylacetate(3) mixtures; the equilibrium composition $x_{1,eq}$ = 0.30, $x_{2,eq}$ = 0.275 and $x_{3,eq}$ = 0.425. Modeling and computational details are provided in Chapter 6 of the Supplementary Material.

for a range of bubble residence times, in agreement with the experimental findings.

The Maxwell-Stefan-Geddes model calculations for distillation of water(1)/ethanol(2)/tert-butanol(3) mixtures show large negative values of E_3; see Fig. 15b. The simulations in Fig. 15b are representative of Run M46 of the experiments of (Krishna et al., 1977) for distillation of this mixture in a sieve tray distillation column, for which negative efficiencies for tert-butanol were reported. For distillation of acetone(1)/chloroform(2)/methanol(3), $E_1 < 0$ and acetone is dragged uphill by its partner species; see Fig. 15c.

The phenomenon of uphill diffusion can be exploited to separate 2-propanol/water, ethanol/water, and acetone/methanol mixtures of azeotropic composition by distillation in the presence of an inert gas such as nitrogen, argon, or helium (Fullarton and Schlünder, 1986; Krishna, 2016b, 2017a; Singh and Prasad, 2011).

Unequal component Murphree efficiencies have important consequences in the design of distillation columns, with strict purity requirements for distillates and residues (Krishna, 2016b; Taylor et al., 2003). As demonstration, we consider the design of sieve-tray distillations for separation of water/ethanol/acetone mixtures. Two different feed compositions are chosen, either side of the distillation boundary; see Fig. 16a,b. For feed on the left side of the distillation boundary, the feed was introduced in such a way that 20% of all column-stages were located above the feed stage. In this case, a purity level of 96% ethanol in the bottom product is specified. For feed on the right side of the distillation boundary, the feed tray was located exactly halfway through the distillation column. In this case, a purity level of 100% water in the bottom product is specified.

The column design was performed with two different modeling approaches: (a) NEQ model, in the vapor and liquid phase transfers were described using the M−S formulation, and (b) the EQ model with component stage efficiencies equal for all species; the efficiency value is chosen as the average of that calculated by the NEQ model (these values are plotted in Fig. 16c and d), averaged over all the trays. The simulations were carried out using ChemSep

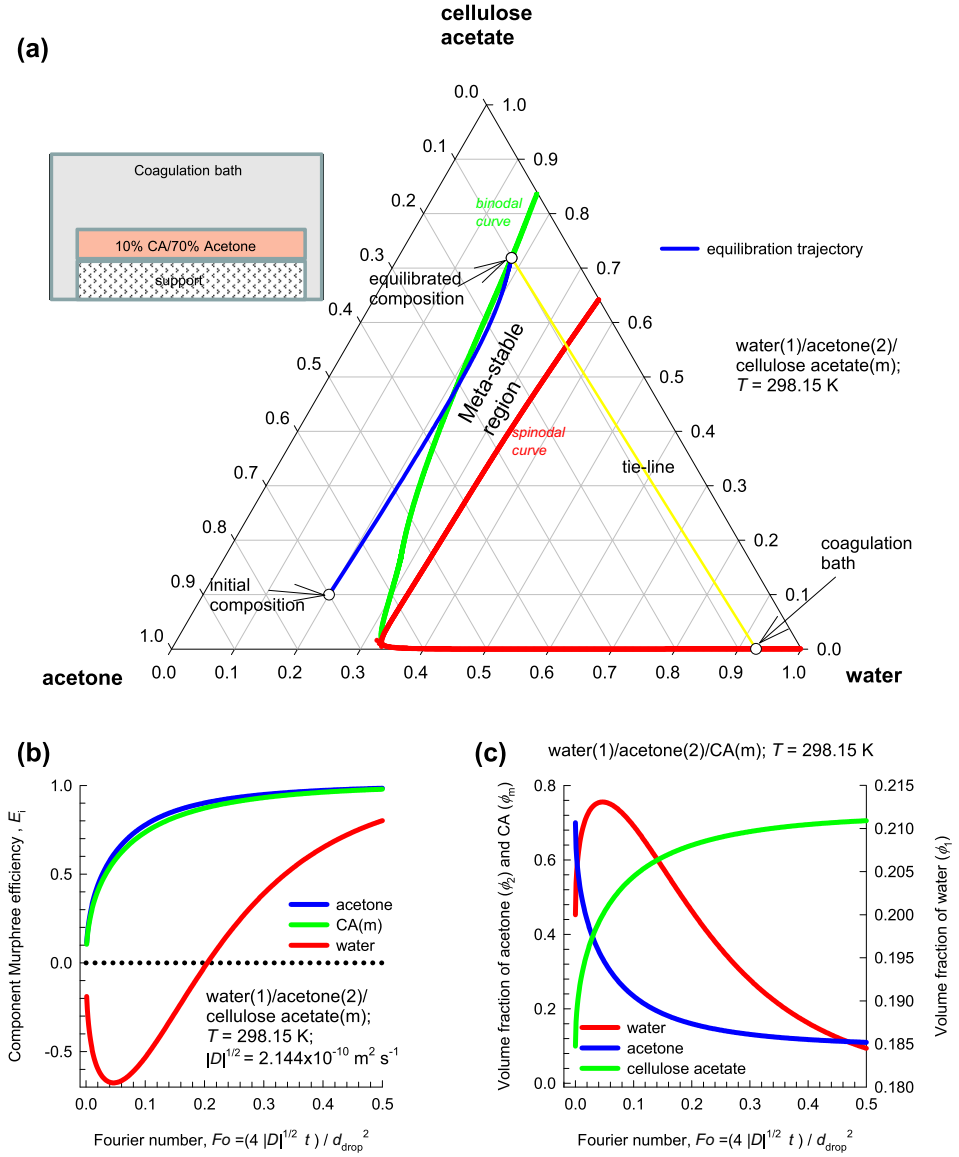

Fig. 21. (a) Geddes equilibration trajectory in a ternary system consisting of water (non-solvent, component 1), acetone (solvent, component 2) and cellulose acetate (polymer, component m). The plotted data in ternary composition space are in terms of volume fractions. The equilibration trajectory is indicated by the blue line in ternary composition space. (b) Plot of the component Murphree efficiencies, E_i, as function of the Fourier number. (c) Transient volume fraction profiles in the polymer solution, as function of the Fourier number. Modeling and computational details are provided in Chapter 7 of the Supplementary Material. (For interpretation of the references to colour in this figure legend, the reader is referred to the web version of this article.)

developed by (Kooijman and Taylor, 2007). The column composition profiles for the NEQ and EQ models are shown in Fig. 16a and b for the two different feed compositions. For the purity requirement of 96% ethanol in the reboiler, the NEQ model requires 39 stages. The EQ model (with equal component efficiencies) requires only 25 stages to attain this product purity. The reason for the extra stages required by the NEQ is evident on examination of the column composition trajectory in Fig. 16a. The NEQ trajectory appears to veer towards the water vertex because of the higher component efficiency of water (cf. Fig. 16c). Water is the least volatile of the three components, and its transfer is directed from vapor to the liquid phase; a higher efficiency of water ensures that the liquid phase is richer in water than anticipated on the basis of equal component efficiencies.

For the feed mixture right of the distillation boundary, the results are shown in Fig. 16b. In this case, the NEQ model requires 30 stages to reach 100% water purity in the bottoms product; the EQ model (with equal component efficiencies) requires 38 trays to reach the same purity target. Due to the higher component efficiency of water (cf. Fig. 16d), the composition trajectory followed by the NEQ model veers towards the water vertex and consequently demands fewer number of stages. In other words, the NEQ model takes a shorter route, and the EQ model follows the scenic route in the column.

The overall conclusion to be drawn from the design study is that use of the conventional EQ model may be either overly optimistic or pessimistic, depending on the feed location, and purity demands. Indeed, the shortcomings of the EQ model were underscored already in 1925 by (Murphree, 1925), who remarked "The concept of the theoretical plate does not offer a satisfactory basis of calculation for rectifying columns when the mixture being rectified contains more than two components..."

7. Murphree efficiencies in ternary liquid extraction

The design and sizing of appropriate liquid-liquid contacting devices such as stirred vessels, sieve-tray columns, and rotating disc contactors are crucially dependent on accurate estimation of the interphase transfer fluxes, and stage efficiencies (Bart, 2001; Kooijman and Taylor, 2007; Lao et al., 1989; Seader et al., 2011; Sherwood et al., 1975; Wankat, 2012). By its very nature, liquid-liquid extraction processes operate in composition regions in the proximity of liquid-liquid phase transitions. An important consequence is that the phase equilibrium thermodynamics has a dominating influence on the diffusivity characteristics, making the interphase mass transfer process strongly coupled, as evidenced by published experimental data (Cullinan and Ram, 1976; Haeberl and Blass, 1999; Krishna et al., 1985; Sethy and Cullinan, 1975). A further consequence of diffusional coupling effects is that the flux of a species need not be directed down its mole fraction

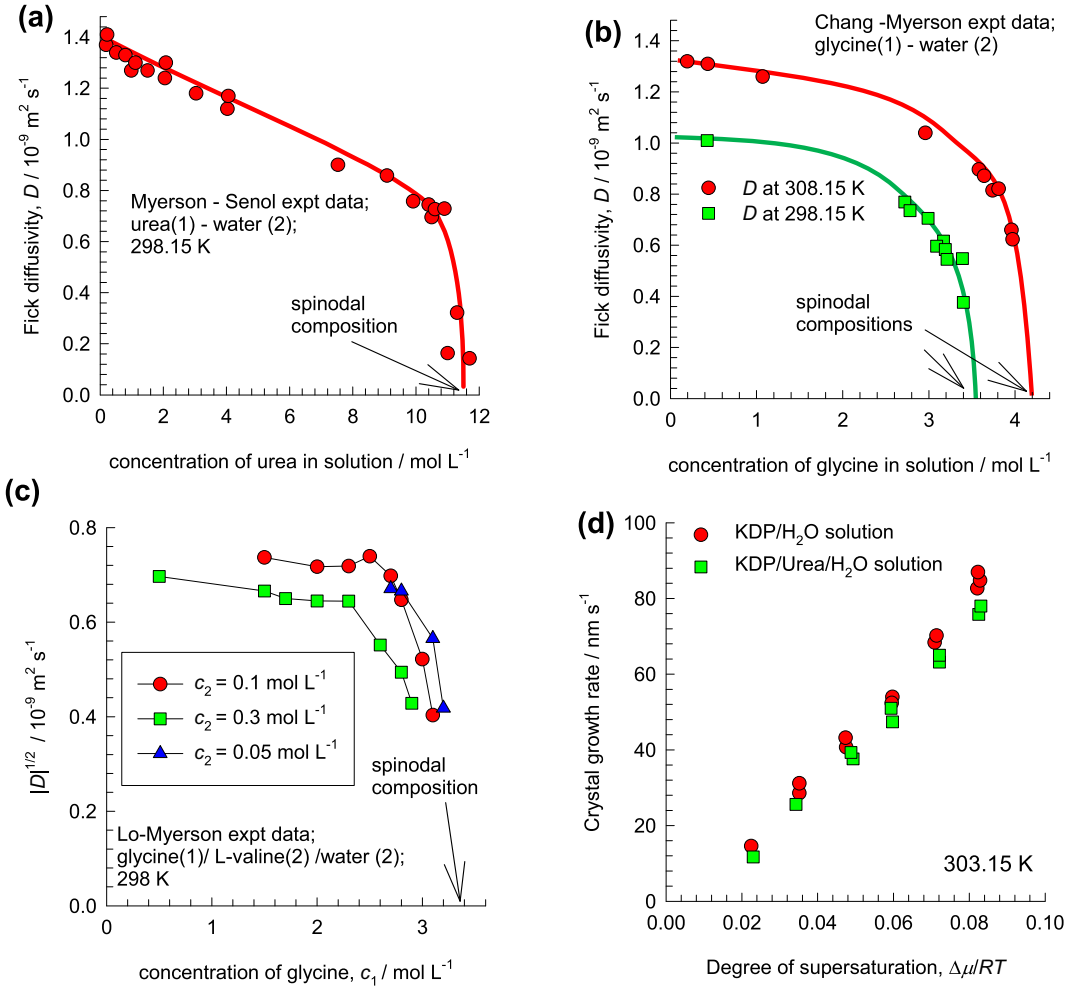

Fig. 22. (a) Fick diffusivity of urea as a function of solute concentration in aqueous solutions, at $T = 298.15$ K (Myerson and Senol, 1984). (b) Fick diffusivity of glycine as a function of solute concentration in aqueous solutions, at $T = 298.15$ K and 308.15 K (Chang and Myerson, 1986). (c) Plot of $|D|^{1/2}$ for glycine(1)/L-valine(2)/water(3) solutions as a function of the molar concentration of glycine, c_1; the data on the Fick diffusivity matrix $[D]$ are culled from (Lo and Myerson, 1989). (d) Experimental data of (Enqvist et al., 2003) on growth rate of KDP crystals as a function of the degree of supersaturation. Further details are provided in Chapter 10 of the Supplementary Material.

gradient. Below, we demonstrate the occurrence of uphill transport in liquid extraction.

Consider the separation a 50/50 propylbenzene/dodecane feed mixture, indicated by F in Fig. 17a. Addition of the extraction agent, N-methyl pyrrolidone (NMP = solvent S) to the feed mixture F results in a mixture of composition M that falls within the unstable region of the phase diagram. The mixture M separates into two phases with compositions E (Extract) and R (Raffinate) at either ends of the tie-line shown. The composition of the extract phase (E) is $x_{1,eq} = 0.6825$, $x_{2,eq} = 0.1955$, and $x_{3,eq} = 0.1220$; the composition of the raffinate phase, at the other end of the tie-line (R) is: $x_{1,eq} = 0.3384$, $x_{2,eq} = 0.2387$, and $x_{3,eq} = 0.4229$. The feed phase F will equilibrate to R, and the solvent phase S will equilibrate to E. In the extract phase E, the propylbenzene/dodecane ratio is 1.6, whereas this ratio is reduced to 0.56 in the raffinate phase R.

We investigate the F-R equilibration trajectory, using the assumption that the 50/50 propylbenzene/dodecane feed mixture is dispersed as droplets of 2 mm diameter in a continuous phase consisting of solvent rich phase. In our calculations we assume that the mass transfer resistance resides predominantly within the dispersed phase; this is a common occurrence (Krishna, 2016b; Sun et al., 2014). The Fick diffusivity matrix, calculated using Eq. (14) at the arithmetic average composition of the dispersed phase droplets between the initial and final equilibrated compositions ($x_{1,av} = 0.1692$, $x_{2,av} = 0.3693$, and $x_{3,av} = 0.4615$) is $[D] = |\Lambda|^{1/2}[\Gamma] = \begin{bmatrix} 0.5151 & -0.2920 \\ -0.1780 & 1.203 \end{bmatrix} \times 10^{-9} m^2 s^{-1}$. The off-diagonal element D_{12} has the same order of magnitude as the diagonal element D_{11}, indicating that coupled diffusion phenomena cannot be ignored. The component driving forces for transfer of NMP (1) and propylbenzene (2) are $\Delta x_1 = x_{10} - x_{1,eq} = -0.3384$, $\Delta x_2 = x_{20} - x_{2,eq} = 0.2613$. Particularly noteworthy is that the driving force for propylbenzene transfer is of the same order of magnitude as that of NMP, but opposite in sign.

The transient equilibration process inside a spherical droplet is described by the (Geddes, 1946) model, Eq. (23). The transient Geddes equilibration trajectory follows a highly curvilinear path to equilibrium; see Fig. 17a. If coupling effects are completely ignored, the equilibration trajectory follows a linear path in composition space.

Fig. 17b presents a plot of component Murphree efficiencies as a function of the dimensionless Fourier number. During the early stages of the equilibration process, the Murphree point efficiency of dodecane (component 2) exhibits negative values, indicative of uphill diffusion. As a consequence of uphill diffusion, the transient equilibration of dodecane exhibits a perceptible composition overshoot during its approach to equilibration; see Fig. 17c.

We now apply the Geddes equilibration model to investigate the equilibration of dispersed droplets in water(1)/chloroform(2)/acetic-acid(3) mixtures; see Fig. 18a. The initial mole fractions of the dispersed phase droplet is $x_{10} = 0.0$, $x_{20} = 0.3$, and $x_{30} = 0.7$. The final equilibrated composition is $x_{1,eq} = 0.2674$, $x_{2,eq} = 0.3822$, and $x_{3,eq} = 0.3504$. The continuous phase has the compositions at the other end of the tie-line: $x_{1,eq} = 0.6100$, $x_{2,eq} = 0.0816$, and $x_{3,eq} = 0.3084$.

The matrix of Fick diffusivity matrix, calculated using Eq. (14) at the arithmetic average composition of the dispersed phase droplets between the initial and final equilibrated compositions ($x_{1,av} = 0.1337$, $x_{2,av} = 0.3411$, and $x_{3,av} = 0.5252$) is $[D] = |\Lambda|^{1/2}[\Gamma] = \begin{bmatrix} 0.8933 & 0.3612 \\ 0.7196 & 0.9407 \end{bmatrix} \times 10^{-9} m^2 s^{-1}$. Both off-diagonal elements are significantly large, indicating strongly coupled diffusion process. The component driving forces for transfer of water (1) and chloroform (2) are $\Delta x_1 = x_{10} - x_{1,eq} = -0.267384$, $\Delta x_2 = x_{20} - x_{2,eq} = -0.08219$. Particularly noteworthy is that the magnitude of the driving force for chloroform transfer is significantly lower than that for water. The transient Geddes equilibration trajectory follows a highly curvilinear path to equilibrium; see Fig. 18a. If coupling effects are completely ignored, the equilibration trajectory follows a linear path in composition space.

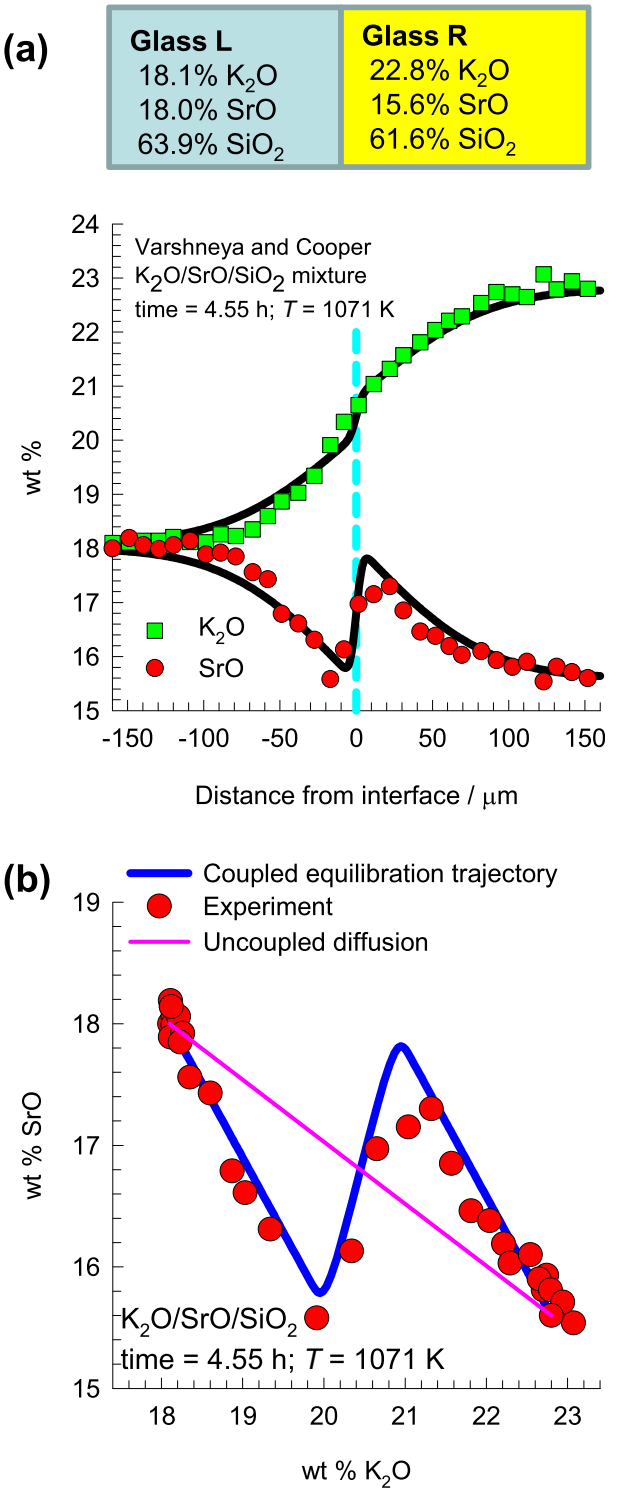

Fig. 23. (a) Experimental data of (Varshneya and Cooper, 1972) for inter-diffusion between the left and right slabs consisting of $K_2O/SrO/SiO_2$ mixtures. The wt% of each component is measured on either side of the Matano plane, measured at $t = 4.55$ h after the start of the experiment are shown. (b) Equilibration trajectories in composition space. Modeling and computational details are provided in Chapter 8 of the Supplementary Material.

Fig. 18b presents a plot of component Murphree efficiencies as a function of the dimensionless Fourier number. During the early stages of the equilibration process, the Murphree point efficiency of chloroform (component 2) exhibits values exceeding unity. As a consequence of uphill diffusion, the transient equilibration of chloroform exhibits a pronounced mole fraction overshoot during its approach to equilibration; see Fig. 18c. It is noteworthy that the transient equilibration process in terms of component activity, $a_i = \gamma_i x_i$ is monotonic; this implies that the composition overshoot of chloroform has its origins in the thermodynamic influences engendered by the off-diagonal elements of $[\Gamma]$.

Analyses of transient equilibration within dispersed droplets of the six other partially miscible ternary liquid mixtures (NMP/propylbenzene/tetradecane, water/acetone/ethyl-acetate, water/-caprolactam/toluene, water/ethanol/benzene, water/ethylacetate/ethanol, and furfural/formic acid/water mixtures) are presented in Chapter 5 of Supplementary material. In all cases, the transient equilibration process show transient overshoot in the composition of one component for which the Murphree efficiency E_i is either <0 or >1. It may be concluded that coupled diffusion and uphill transport may be expected to be the norm rather than the exception in liquid extraction processes.

Uphill diffusion is also to be expected for transfers in near-critical and super-critical fluid mixtures under conditions relevant to enhanced oil recovery processes (He and Ghoniem, 2018).

8. Forays into meta-stable regions, emulsification, and the Ouzo effect

The aniseed-based alcoholic beverage Ouzo consists of a three component mixture of ethanol (≈45 vol%), water (55 vol%) and an essential oil called trans-anethol (≈0.1%) (Grillo, 2003). It is commonly consumed with the addition of three to five volumes of water to one volume of Ouzo; see Fig. 19. From the phase equilibrium diagram it appears that the inter-mixing of Ouzo and water must follow a non-linear composition trajectory in order to enter the meta-stable zone in which the oil spontaneously nucleates into tiny droplets (Ganachaud and Katz, 2005; Sitnikova et al., 2005). The tiny 1 nm sized droplets scatter light, causing the drink to appear milky white. (Vitale and Katz, 2003) have coined the generic term "Ouzo effect" to describe such a process of creating meta-stable liquid-liquid dispersions. Since no input of mechanical energy is involved, this offers an energy-efficient method of producing nanospheres and nanoparticles (Ganachaud and Katz, 2005; Haase and Brujic, 2014; Solans et al., 2016).

As illustration of the Ouzo effect, consider inter-diffusion between two compartments containing water(1)/acetone(2)/ethy lacetate(3) mixtures. The initial composition of the left compartment is: $x_{1,L} = 0.05$, $x_{2,L} = 0.1$ and $x_{3,L} = 0.85$; the initial composition of the right compartment is: $x_{1,R} = 0.55$, $x_{2,R} = 0.45$ and $x_{3,R} = 0.0$. The composition at equilibrium is $x_{1,eq} = 0.3$, $x_{2,eq} = 0.275$ and $x_{3,eq} = 0.425$; this point lies on the binodal curve. The matrix of thermodynamic factors, calculated at the arithmetic average compositions is $[\Gamma] = \begin{bmatrix} 0.169614 & -0.365349 \\ 0.085606 & 1.270447 \end{bmatrix}$. The matrix of Fick diffusivity matrix, calculated using Eq. (14), yielding $[D] = |\Lambda|^{1/2}[\Gamma] = \begin{bmatrix} 0.34674 & -0.746879 \\ 0.175003 & 2.59716 \end{bmatrix} \times 10^{-9} m^2 s^{-1}$. The off-diagonal element D_{12} is a significantly large fraction of the diagonal element D_{11}, indicating strongly coupled diffusion flux of water with the acetone driving force. Fig. 20 shows that the equilibration trajectory in the right chamber has forayed into the meta-stable region; this foray is primarily engendered by uphill diffusion of water. It is noteworthy that in the classic paper by (Ruschak and Miller, 1972), linear equilibration trajectories are used to predict spontaneous emulsification; use of this approach will not anticipate any foray into the meta-stable region.

We now demonstrate that the foray into the meta-stable regions of water/acetone/cellulose acetate mixtures as witnessed in Fig. 3 is caused by uphill diffusion. Towards this end, we consider transient diffusion within a spherical droplet that is dispersed in a continuous phase that is representative of the coagulation bath in the immersion precipitation process. The initial volume fractions in the drop are $\phi_{10} = 0.2$, $\phi_{20} = 0.7$, and $\phi_{30} = 0.1$. The final equilibrated composition is $\phi_{1,eq} = 0.18067$, $\phi_{2,eq} = 0.10078$, and $\phi_{3,eq} = 0.71855$; this composition is in equilibrium with the solution in the coagulation bath, maintained at constant composition.

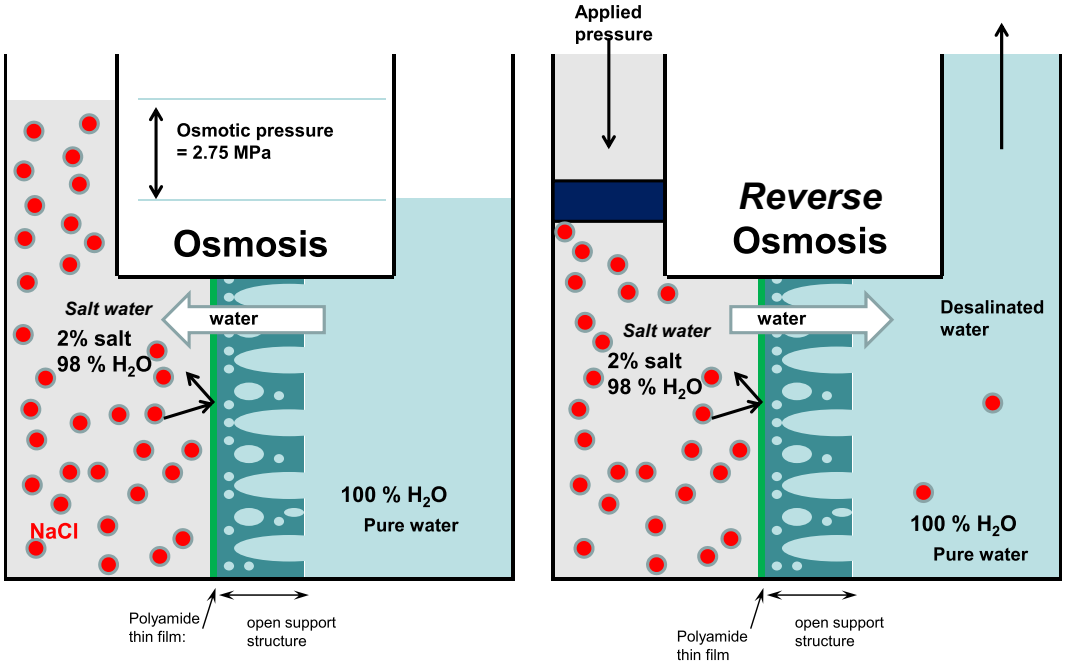

Fig. 24. Water transport across polyamide-based reverse osmosis membrane, (). adapted from Wesselingh and Krishna, 2000

The matrix of thermodynamic factors, calculated using the Flory-Huggins model at the arithmetic average volume fractions of the dispersed phase droplets between the initial and final equilibrated compositions ($\phi_{1,av} = 0.19034$, $\phi_{2,av} = 0.40039$, and $\phi_{3,av} = 0.40927$) is $[\Gamma] = \begin{bmatrix} 0.34018 & -0.06198 \\ -0.78883 & 0.60362 \end{bmatrix}$. Using the M–S diffusivity data from (Mulder and Smolders, 1984) the Fick diffusivity matrix is estimated as $[D] = \begin{bmatrix} 2.23353 & -0.40692 \\ -3.53135 & 2.7022 \end{bmatrix} \times 10^{-10}$ m^2 s^{-1}. The component driving forces for transfer of water (1) and acetone (2) are $\Delta\phi_1 = \phi_{10} - \phi_{1,eq} = 0.01933$, and $\Delta\phi_2 = \phi_{20} - \phi_{2,eq} = 0.59922$. From Eq. (7), we conclude that the fluxes of water and acetone are strongly coupled to each other.

The transient Geddes equilibration trajectory follows a curvilinear path to equilibrium, and exhibits a foray into the meta-stable region; see Fig. 21a.

Fig. 21b presents a plot of component Murphree efficiencies as a function of the dimensionless Fourier number. During the early stages of the equilibration process, the Murphree point efficiency of water (component 1) exhibits negative values, indicative of uphill diffusion. As a consequence of uphill diffusion, the transient equilibration of water exhibits a distinct composition overshoot during its approach to equilibration; see Fig. 21c. Indeed, uphill diffusion of water causes the trajectory to veer into the meta-stable region. For more detailed modeling of the immersion precipitation processes, see (Reuvers and Smolders, 1987; Tsay and McHugh, 1990; van den Berg and Smolders, 1992).

9. Kinetics of crystal growth

Molecular diffusion near meta-stable and supersaturation regions is of crucial importance in determining the kinetics of crystal growth (Garside, 1985). The diffusivity of urea, and glycine in water plummets to vanishingly low values as the spinodal compositions, indicated by the arrows in Fig. 22a,b, are reached. The strong concentration dependence of the Fick diffusivity is dictated by the thermodynamic factor Γ, that vanishes at the spinodal composition. (Lo and Myerson, 1989) report data on the Fick diffusivity matrix $[D]$ for glycine(1)/L-valine(2)/water(3) solutions. Fig. 22c presents a plot of $|D|^{1/2}$ as a function of the molar concentration of glycine, c_1; the magnitude of $|D|^{1/2}$ tends to vanish as the spinodal compositions are approached, as anticipated by Eq. (13); consequently diffusional coupling effects will be of crucial importance in crystal growth kinetics. To model crystal growth kinetics it is common practice to use the chemical potential difference between the supersaturated solution (the transferring state) and the crystal (the transferred state), $\left(\mu_i - \mu_{i,eq}\right)/RT = \ln\left(a_i/a_{i,eq}\right)$, as the driving force and is commonly referred to as the degree of supersaturation (Garside, 1985; Louhi-Kultanen et al., 2001).

As a good approximation, the Potassium Dihydrogen Phosphate (KDP) growth rate is proportional to the activity based degree of supersaturation. As illustration, Fig. 22d presents the experimental data on growth rate of KDP crystals, at the **[1 0 1]** face, as function of $\Delta\mu/RT$. (Louhi-Kultanen et al., 2001) present a detailed model for growth of KDP crystals in aqueous solutions of mixed electrolytes using the M–S formulation, along with the Pitzer model for activity coefficients. Further modelling details are provided in Chapter 10 of the Supplementary Material.

10. Uphill diffusion in crystalline solids, alloys, and glasses

In a set of experiments reported by (Varshneya and Cooper, 1972), two glass slabs with different compositions of $K_2O/SrO/SiO_2$ were brought into contact at time $t = 0$ and the transient concentration distributions determined. The wt% of each component, measured at $t = 4.55$ h after the start of the experiment are shown in Fig. 23a. The over- and under-shoots in the SrO concentrations are noteworthy. The non-monotonous equilibration trajectory observed for SrO signals uphill diffusion; such phenomena are of

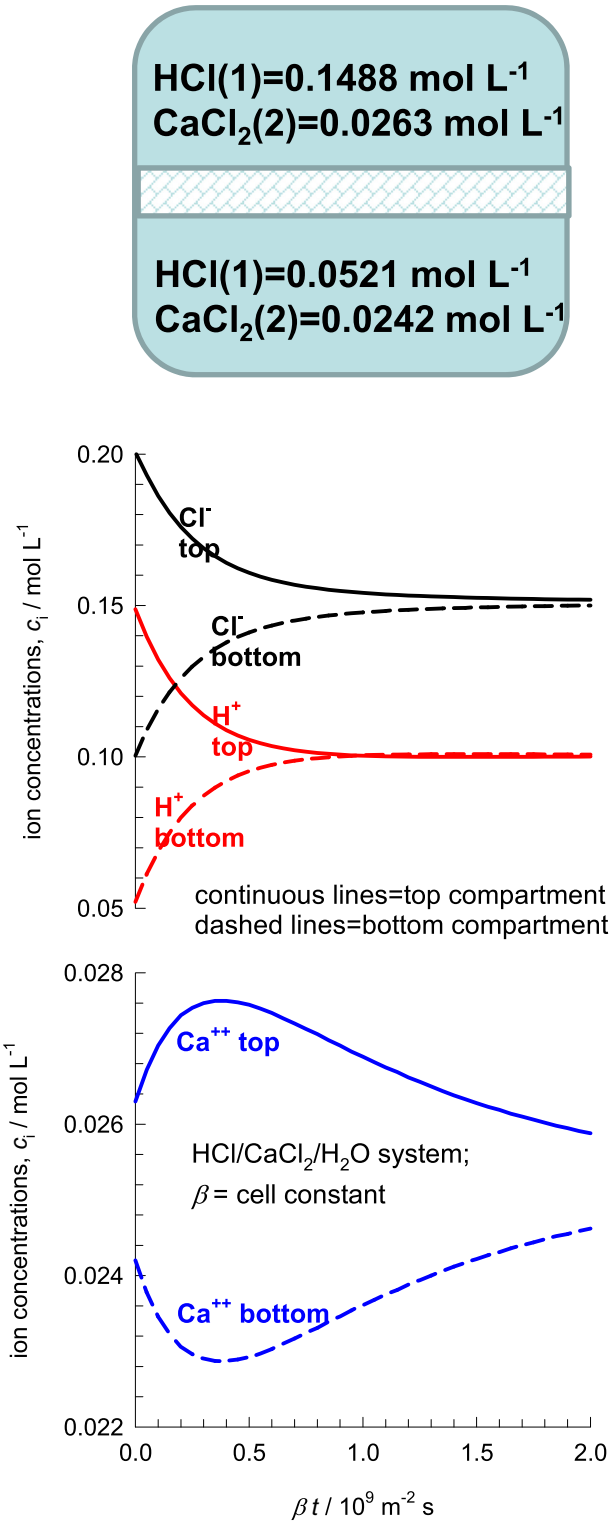

Fig. 25. Transient approach to equilibrium of the concentrations of H^+, Ca^{++}, and Cl^- in the top and bottom compartments separated by a diaphragm. Modeling and computational details are provided in Chapter 10 of the Supplementary Material.

importance in the processing of ceramics, cements, alloys, steels, and composites (Ågren, 2012; Christensen, 1977; Glicksman, 2000; Gupta and Cooper, 1971; Vielzeuf and Saúl, 2011). The over- and under-shoots in the SrO concentrations signal the phenomenon of uphill diffusion; these are adequately modeled with the Fick matrix $[D] = \begin{bmatrix} 1 & -0.267 \\ -1.22 & 0.33 \end{bmatrix} \times 10^{-13}$ m^2 s^{-1}. The large off-diagonal contributions are attributable to the influence of $[\Gamma]$. The transient equilibration process, plotted in composition space follows a serpentine trajectory; see Fig. 23b. Use Eq. (1) will yield a linear equilibration trajectory. Uphill diffusion can be gainfully exploited to modify the surface properties of alloys and glasses (Ågren, 2012; Glicksman, 2000).

Detailed analysis of transient equilibration in PbS/PbTe/PbSe, C/Si/Fe, Co/Fe/Ni, and Fe/Mg/Ca mixtures, presented in Chapter 8 of Supplementary material also confirm that the origins of uphill diffusion are traceable to the sizable off-diagonal elements of the Fick diffusivity matrix $[D]$, engendered by thermodynamic non-idealities.

11. Reverse osmosis

The best known example of uphill diffusion is in the reverse osmosis process for desalination in which fresh water is recovered from saline water by use of a polyamide film membrane that rejects salt, and only allows water to permeate (Sirkar, 2014; Wankat, 2012); see Fig. 24. The transport of water occurs from the compartment with salt water (typically 98% water), on the left of the membrane to a region with nearly 100% pure water, on the right side. In reverse osmosis, the driving force for transport across the polyamide membrane layer must additionally account for the contribution of the pressure gradients. The expression for the water transport velocity, u_w, across the membrane is obtained by modifying Eq. (2) as follows

$$-\frac{d\mu_w}{dz} - \bar{V}_w \frac{dp}{dz} = \frac{RTu_w}{Đ_{wM}} \tag{24}$$

where $\bar{V}_w$ is the partial molar volume of water, and $Đ_{wM}$ reflects the interaction between water and the membrane (M). In Eq. (24), we neglect diffusional interactions between water and salt. Ignoring thermodynamic non-ideality effects, we can re-write Eq. (24) in the following form for a membrane of thickness δ

$$-\frac{\Delta x_w}{\delta} - \frac{1}{RT}\bar{V}_w \frac{\Delta p}{\delta} = \frac{u_w}{Đ_{wM}} \tag{25}$$

In desalination operations, the upstream compartment will typically have 2 mol % salt and the downstream compartment will be practically salt-free. Therefore, the driving force for water transport $\Delta x_w = 1.0 - 0.98 = 0.02$. If no additional pressure is applied to the upstream compartment, the pressure difference at equilibrium, corresponding to $u_w = 0$, is called the osmotic pressure

$$\Delta p = -\frac{RT\Delta x_w}{\bar{V}_w} \tag{26}$$

Typically, T = 298 K, and $\bar{V}_w = 1.8 \times 10^{-5}$ m^3 mol^{-1}; the osmotic pressure is 2.75 MPa. In order to drive water from the left to right in Fig. 24, we need to apply Δp values exceeding 2.75 MPa. In reverse osmosis operations, water is literally "pumped" uphill by application of Δp. For all other examples presented in this article, no physical "pump" is employed.

12. Uphill diffusion in aqueous electrolyte solutions

For transport of ionic species in electrolyte solutions we need to augment the left member of Eq. (2) by addition the contribution of the electrostatic potential gradient (Lightfoot, 1974; Newman and Thomas-Alyea, 2004)

$$-\frac{d\mu_i}{dz} - z_i F \frac{d\Phi}{dz} = \sum_{j=1\, j\neq i}^{n} \frac{RT}{Đ_{ij}} x_j (u_i - u_j); \quad i = 1, 2..n \tag{27}$$

where z_i is the ionic charge of species i and F is the Faraday constant. If ion-ion interactions are neglected, Eq. (27) simplifies to

$$N_i = -Đ_i \frac{c_i}{RT}\frac{d\mu_i}{dz} - c_i z_i Đ_i \frac{F}{RT}\frac{d\Phi}{dz} + c_i u_n; \qquad i = 1, 2, \ldots n-1 \tag{28}$$

where the $Đ_i$ are the ion-solvent M−S diffusivities and the ionic diffusion fluxes are defined as

$$N_i = c_i u_i; \quad i = 1, 2, \ldots n \tag{29}$$

The species n is often water, that is usually present in significantly large proportions, and can often be considered stagnant, $N_n = c_n u_n = 0$. For dilute aqueous solutions of electrolytes, the activity coefficients are approximately unity, so $\frac{c_i}{RT}\frac{d\mu_i}{dz} \approx \frac{dc_i}{dz}$. For dilute solutions, Eq. (28) reduce to the Nernst-Planck equations

$$N_i = -Đ_i \frac{dc_i}{dz} - c_i z_i Đ_i \frac{F}{RT}\frac{d\Phi}{dz}; \qquad i = 1, 2, \ldots n-1 \tag{30}$$

Except in regions close to electrode surfaces, where there will be charge separation (the double layer phenomena), the condition of electro-neutrality is met

$$\sum_{i=1}^{n} z_i c_i = 0; \quad \sum_{i=1}^{n-1} z_i \frac{dc_i}{dz} = 0; \quad \text{electroneutrality constraint} \tag{31}$$

The total current carried by the electrolyte is $F\sum_{i=1}^{n} z_i N_i$. In many chemical process applications such as ion exchange, no external electrical field is imposed on the system, and also there is no flow of current, i.e.

$$\sum_{i=1}^{n} z_i N_i = 0; \quad \text{no current prescription} \tag{32}$$

The electro-neturality constraint (31) causes the ionic fluxes to be strongly coupled even in dilute electrolyte solutions. The second right member of Eq. (30) serves as an electrostatic leash, that acts in a manner to either accelerate or decelerate a specific ion, even transporting it uphill. Evidence of uphill diffusion is presented by (Nakagaki and Kitagawa, 1976) who conducted transient inter-diffusion experiments in $HCl/CaCl_2/H_2O$ aqueous solutions in a diaphragm cell with two well-stirred compartments. The top and bottom comparments are initially filled with two distinctly different concentrations of the two aqueous electrolyte solutions, HCl, and $CaCl_2$. In one of their experiments, the top compartment contains HCl and $CaCl_2$ with concentrations of 0.1488 mol L^{-1} and 0.0263 mol L^{-1}, respectively. The initial concentrations of HCl and $CaCl_2$ in the bottom compartment are 0.0521 mol L^{-1} and 0.0242 mol L^{-1}, respectively. Each of the electrolytes will undergo complete dissociation. The transient equilibration process can be simulated by combining the Nernst-Planck Eq. (30) with the continuity relations. The concentration evolutions in the top and bottom compartments during transient equilibration are presented in Fig. 25. The diffusion equilibration of H^+, and Cl^- proceeds in a "normal" manner, i.e. the transport is from higher to lower concentration regions with exponential decay. The equilibration of Ca^{++} ions is remarkable in that a concentration overshoot is experienced in the top compartment with a concomitant undershoot in the bot-

tom compartment. Let us explain the concentration overshoot in physical terms. The more mobile H^+ rapidly diffuses into the bottom compartment; this creates an excess of positive charge. This excess of positive charge serves to prevent the influx of Ca^{++} ions into the bottom compartment even though its concentration is higher in the top compartment. Indeed, the requirement of electro-neutrality causes the Ca^{++} ions to traverse uphill from bottom to top compartment. Uphill transport of Ca^{++} ions leads to transient overshoots in the early stages of equilibration. (Nakagaki and Kitagawa, 1976) have reported a negative value for the "effective" ionic diffusivity of Ca^{++} ions in their experiments. Negative effective ionic diffusivities are indicative of uphill ionic transport, engendered by the electro-static "leash".

Other examples of uphill transport in mixed electrolyte solutions containing fully or partially dissociated compounds: HCl/$BaCl_2$, HCl/$CaCl_2$, NaCl/$MgCl_2$, NaCl/$SrCl_2$, NaCl/$MgSO_4$, NaCl/Na_2SO_4/$MgSO_4$, K_2SO_4/KOH, Li_2SO_4/LiOH, LiCl/NaCl/NaOH, LiCl/KCl, HCl/NaOH, Acetic Acid/H_2O and SO_2/$NaHSO_3$ are provided in Chapter 10 of the Supplementary material.

(Sherwood and Wei, 1955) used the Nernst-Planck equations to investigate overall rate of absorption, and instantaneous reaction of HCl into aqueous NaOH. The electro-static leash serves to enhance the rate of absorption by more than twice that predicted by the use of classical Hatta theory as applied to uncharged reactants; see the detailed analysis presented in Chapter 10 of the Supplementary material.

13. Forward/reverse intra-particle ion exchange

We now rationalize and model the set of two experiments shown in Fig. 4a,b. The total concentration of negative charges inside the matrix has a fixed value, c_{fixed}, expressed say as mole equivalent per volume. Typically, the concentration of fixed negative charges is in the range of 1 to 4 mol L^{-1} (Wesselingh and Krishna, 2000); this value is considerably higher than the molar concentrations of ions in the bulk electrolyte solutions surrounding the particle. The concentration of counter ions within the particle must balance c_{fixed} and therefore we have $\sum_{i=1}^{m} z_i c_i = c_{fixed}$ where m is the total number of counter-ions. The quantity $\frac{z_i c_i}{c_{fixed}} \equiv X_i$ is the ionic *equivalent* fraction. The ionic equivalent fractions of the m counter ions sum to unity $\sum_{i=1}^{m} X_i = 1$. The Nernst-Planck flux relations for m counter-ions in IEX resin can be written as

$$z_i N_i = -c_{fixed} Đ_i \frac{dX_i}{dz} - c_{fixed} X_i z_i Đ_i \frac{F}{RT} \frac{d\Phi}{dz}; \quad i = 1, 2, \ldots m \tag{33}$$

where the fluxes are defined in a reference frame with respect to the IEX particle. The corrective action of the induced potential gradient $\frac{d\Phi}{dz}$ is mainly directed *against* the species that is present in the *higher* equivalent fraction X_i.

It is convenient to define an $(m\text{-}1)\text{x}(m-1)$ dimensional square matrix $[D_{eff}]$ (Jones and Carta, 1993; Rodriguez et al., 1998; Yoshida and Kataoka, 1987)

$$z_i N_i = -c_{fixed} \sum_{k=1}^{m-1} D_{ik,eff} \frac{dX_k}{dz}; \quad i = 1, 2, ..m-1 \tag{34}$$

The elements of $[D_{eff}]$ can be derived by applying the no-current $\sum_{i=1}^{m} z_i N_i = 0$ and electro-neutrality $\sum_{i=1}^{m} z_i \frac{dX_i}{\partial z} = 0$ constraints for intra-particle diffusion; the result is

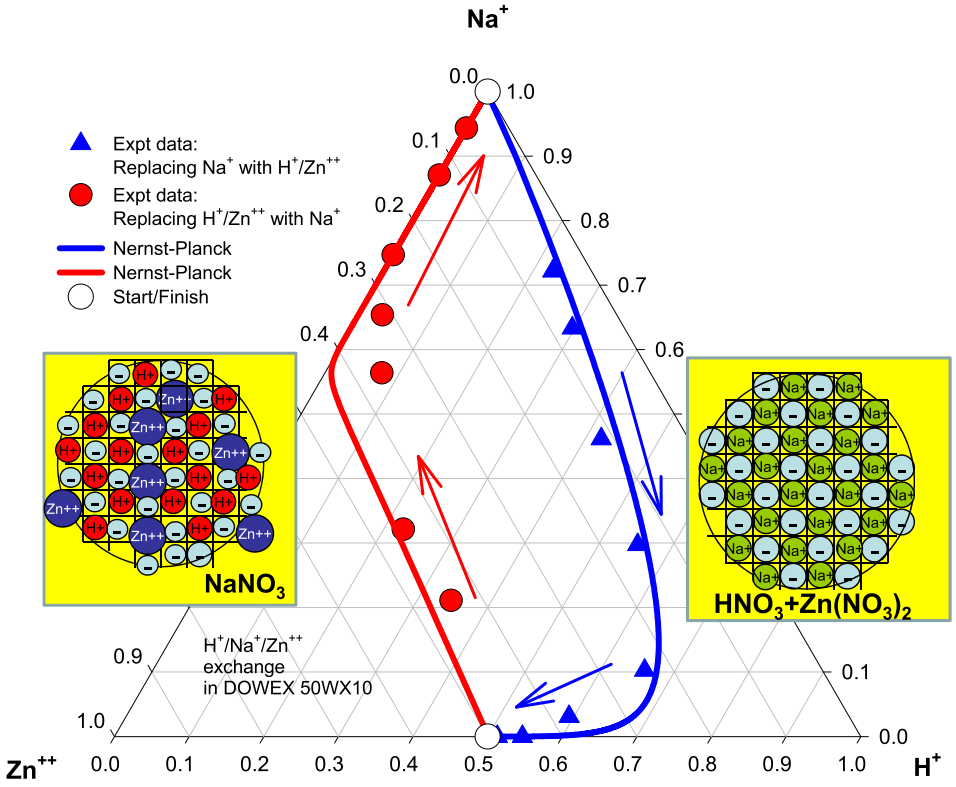

Fig. 26. Plots of the ionic equivalent fractions $\frac{z_i c_i}{c_{fixed}}$ in ternary composition space for transient exchange of $H^+/Na^+/Zn^{++}$ within DOWEX 50WX10 cation exchanger particle of radius 0.4 mm. Two scenarios are simulated. Two scenarios are considered. (a) Initially the particle is loaded with Na^+ and is replaced H^+/Zn^{++}. (b) Initially the particle is loaded with H^+/Zn^{++} and is replaced Na^+. The experimental data in (Yoshida and Kataoka, 1987) are indicated by symbols. The Nernst-Planck-Geddes model simulations are indicated by the continuous solid lines. Modeling and computational details are provided in Chapter 10 of the Supplementary Material; see also (Krishna, 2016a).

$$D_{ik,eff} = Đ_i\delta_{ik} - \frac{(X_i z_i Đ_i)}{\sum_{j=1}^{m} X_j z_j Đ_j}(Đ_k - Đ_m); \quad i,k = 1,2,\ldots m-1 \tag{35}$$

The transient overshoot in the uptake of H^+ witnessed in Fig. 4c is properly captured by the using the Geddes model (Eq. (23)) wherein the Fick diffusivity matrix is calculated using Eq. (35). The H^+ overshoot is engendered by differences in the magnitudes of the ionic diffusivities, and the electrostatic "leash". The model calculations are also in good agreement with the experimental data for the reverse ion exchange process in which the particle is initially loaded with H^+/Zn^{++} and is replaced by Na^+; see Fig. 4d. The equilibration trajectories for the forward/reverse ion exchange follow completely different paths when plotted in composition space; see Fig. 26.

Asymmetry in forward/reverse ion exchange processes also occurs when there are only two counter-ions in the IEX particle; in this case, Eq. (35) degenerates to yield the following expression for the effective diffusivity of either counter-ion

$$D_{eff} = \frac{X_1 z_1 + X_2 z_2}{\left(\frac{X_1 z_1}{Đ_2} + \frac{X_2 z_2}{Đ_1}\right)} \tag{36}$$

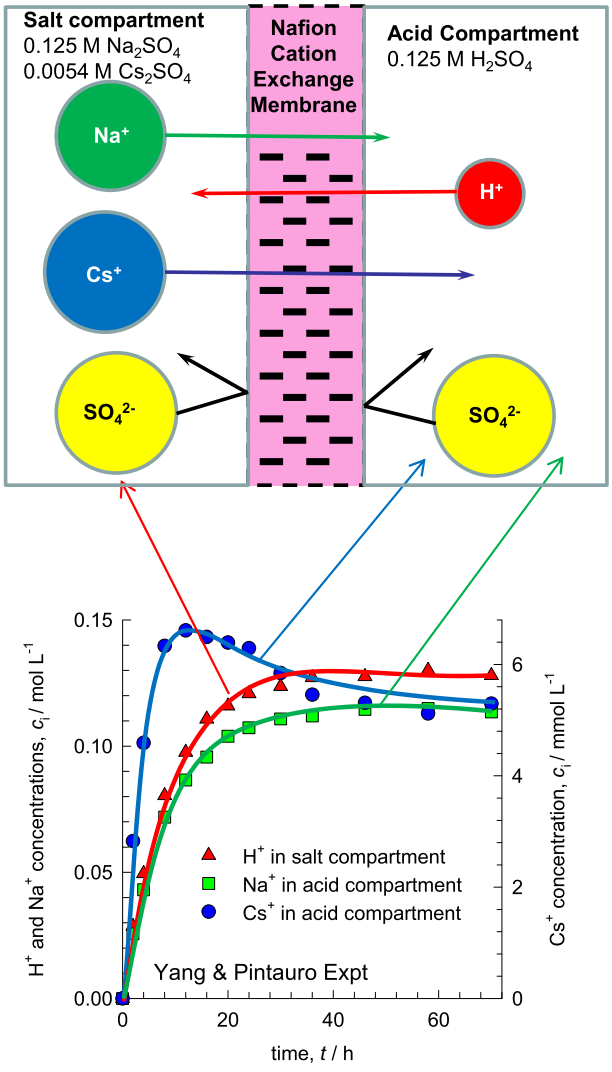

Fig. 27. Experimental data of (Yang and Pintauro, 2000) for the transient equilibration of H^+, Na^+, and Cs^+ in the salt and acid compartments that are separated by a Nafion cation exchange membrane. Modeling and computational details are provided in Chapter 10 of the Supplementary Material; see also (Krishna, 2016a).

For the limiting scenario $X_1 \to 0$, Eq. (36) yields

$$\begin{aligned} X_1 &\to 0; \quad D_{eff} \to Đ_1 \\ X_2 &\to 0; \quad D_{eff} \to Đ_2 \end{aligned} \tag{37}$$

Remarkably, the intra-particle effective diffusivity corresponds to the diffusivity of the ion that is present in the *smaller* quantity. Helfferich, a pioneer in ion exchange, has termed this the "minority rule". To quote (Helfferich, 1983): *binary interdiffusion is not a democratic process but, in the parlance of the activist 1960's, is ruled by a participating minority*! The asymmetry in experiments of (Yoshida and Kataoka, 1987) (cf. Figs. 4, 26) may be viewed as the consequence of the extension of the minority rule to three counter-ions.

14. Transient overshoots for permeation across cation exchange membrane

(Yang and Pintauro, 2000) report a set of experimental data for transient transport of H^+, Na^+, and Cs^+ ions across a Nafion cation exchange membrane separating the acid and salt compartments; see Fig. 27a. The H^+ ions transfer from the acid to the salt compartment. Both Na^+, and Cs^+ ions transfer from the salt to the acid compartment. The SO_4^{2-} ions cannot cross the membrane. Due to the significantly higher mobility of the H^+ ions, there is a significant influence of the diffusion potential $\frac{d\Phi}{dz}$ that tends to influence the mobility of the Na^+, and Cs^+ ions during the initial stages of the transience. Since the concentration driving force of Cs^+ ions is very small, the initial transience is strongly dictated by the diffusion potential; this results in the observed overshoot in the transient equilibration of Cs^+. The transient overshoot can be quantitatively captured using the Nernst-Planck equations; modeling details are provided in Chapter 10 of the Supplementary material.

15. Uphill diffusion in microporous crystalline materials

We now turn to the modeling of the transient uptake experiments shown in Fig. 5. The guest molecules in microporous host materials such as zeolites and metal organic frameworks exist in the adsorbed phase. The force acting per mole of adsorbate species i is balanced by (1) friction between i and the pore walls that are

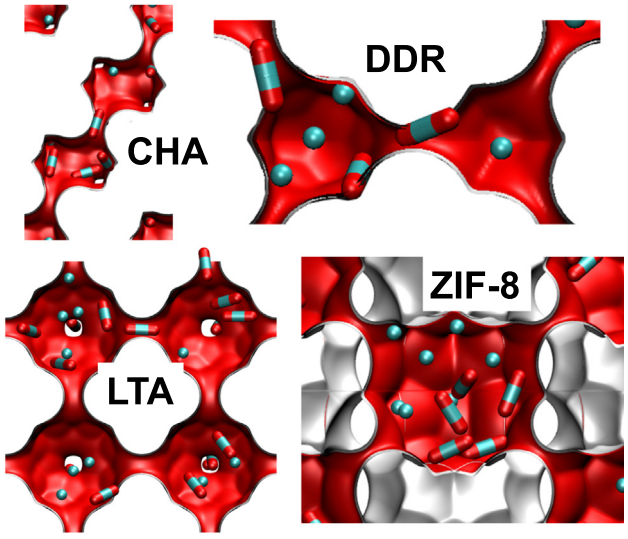

Fig. 28. Snapshot showing the side-ways hopping of CO_2 across the windows of CHA, DDR, LTA, and ZIF-8. Video animations of the molecular hoppings are provided in the Supplementary Material accompanying the paper by (Krishna and van Baten, 2018).

considered to be stationary ($u_w = 0$) and (2) friction between species i and species j. The extension of the M–S Eq. (2) is intuitive (see also Chapter 11 of Supplementary Material for details)

$$-\frac{d\mu_i}{dz} = \sum_{j=1; j\neq i}^{n} \frac{RT}{Đ_{ij}} x_j (u_i - u_j) + \frac{RT}{Đ_i}(u_i); \quad i = 1, 2 \ldots n \tag{38}$$

The x_i in Eqs. (38) represent the component mole fractions in the adsorbed phase within the pores

$$x_i = q_i/q_t; \quad q_t = \sum_{i=1}^{n} q_i; \quad i = 1, 2, ..n \tag{39}$$

where q_i is the molar loading of the adsorbate. The multiplication factor x_j has been introduced in the numerator of the first right member of Eq. (38) because the friction experienced by species i with the each of the other species in the adsorbed phase should be proportional to the relative amounts of species j in the adsorbed phase. If we define the molar fluxes in a reference velocity frame with respect to the pore walls, $N_i = \rho q_i u_i$, we derive (Krishna and van Baten, 2009b)

$$-\rho \frac{q_i}{RT}\frac{d\mu_i}{dz} = \sum_{\substack{j=1 \\ j\neq i}}^{n} \left(\frac{x_j N_i - x_i N_j}{Đ_{ij}}\right) + \frac{N_i}{Đ_i}; \quad i = 1, 2 ... n \tag{40}$$

The $Đ_i$ quantify molecule-wall interactions; they may be interpreted as inverse drag coefficients between the species i and the material surface. For meso- and macro-porous materials, the $Đ_i$ may be identified with the Knudsen diffusivity if the guest molecules have poor adsorption strength (Krishna, 2016c). The $Đ_{ij}$ may be interpreted as the inverse drag coefficient between species i and species j, within the porous framework. At the molecular level, the $Đ_{ij}$ reflect how the facility for transport of species i *correlates* with that of species j; they are also termed *exchange coeffi-*

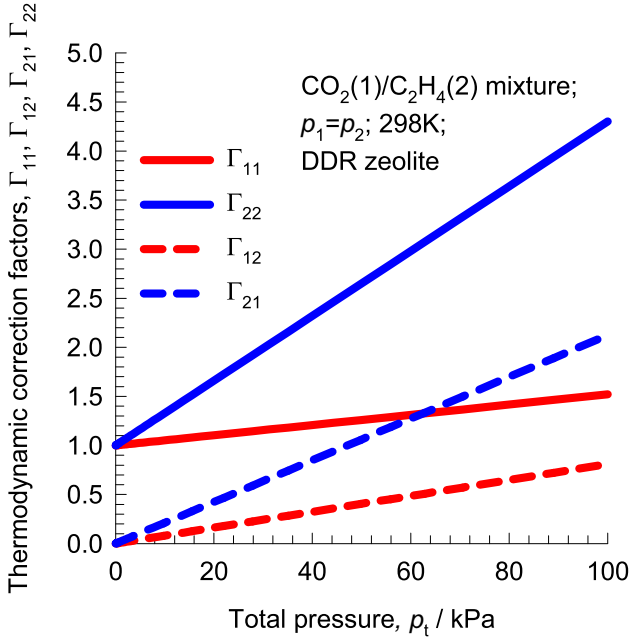

Fig. 29. Elements of the matrix of thermodynamic correction factors Γ_{ij} as a function of total pressure, p_t, for binary $CO_2(1)/C_2H_6(2)$ mixture adsorption in DDR for equal partial pressures in the gas phase. The calculations are based on the mixed-gas Langmuir model; further simulation details are provided by (Krishna, 2016d, 2018).

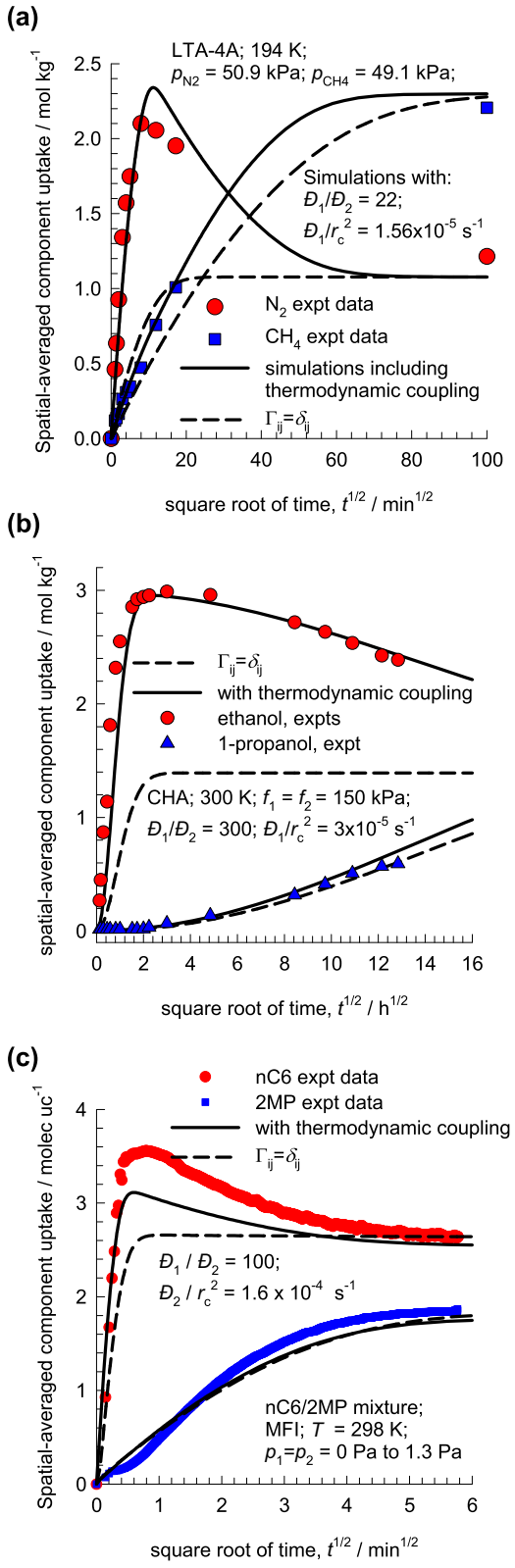

Fig. 30. (a) Experimental data of (Habgood, 1958) on transient uptake of $N_2(1)/CH_4(2)$ mixture within LTA-4A crystals, exposed to binary gas mixtures at 194 K and partial pressures $p_1 = 50.9$ kPa; $p_2 = 49.1$ kPa. (b) Experimental data of (Saint-Remi et al., 2013) for transient uptake of ethanol/1-propanol mixtures within SAPO-34, that is the structural analog of CHA zeolite. (c) Experimental data (Run 1) (Titze et al., 2014) for transient uptake of 50/50 nC6/2MP mixtures in MFI zeolite at 298 K and total pressure of 2.6 Pa. The continuous solid lines are numerical simulations based on the flux Eq. (44). The dashed lines are the calculations using the simplification $\Gamma_{ij} = \delta_{ij}$. Further simulation details are provided by (Krishna, 2016d, 2018).

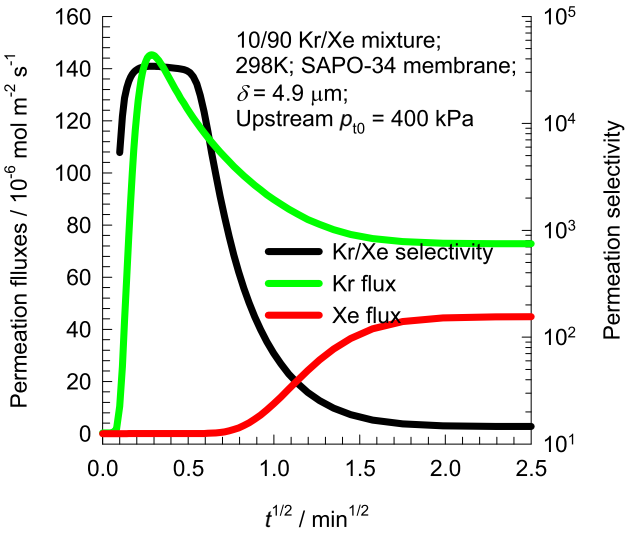

Fig. 31. Transient permeation of 10/90 Kr (1)/Xe (2) across SAPO-34 membrane of thickness δ= 4.9 μm at upstream total pressure of 400 kPa, and T = 298 K. Further simulation details are provided by (Krishna, 2017b).

cients. For mesoporous and macroporous materials, the $Đ_{ij}$ can be identified with the corresponding diffusivity of the bulk fluid mixture (Krishna, 2016c; Krishna and van Baten, 2009a, 2009b).

Correlation effects are of negligible importance for mixture diffusion in cage-type host materialss such as LTA, DDR, CHA, ERI, and ZIF-8 that consist of cages separated by narrow windows in the 3.3–4.4 Å size range. In such cage-window structures the guest molecules hop one-at-a-time between cages (Krishna, 2009, 2012; Krishna and van Baten, 2011; Krishna and van Baten, 2013); making the inter-cage hops uncorrelated. As illustration Fig. 28 presents computational snapshots of lengthwise jumping of pencil-like CO_2 molecule across the windows of CHA, DDR, LTA, and ZIF-8. In cage-window structures, we have $Đ_1 << Đ_{12}$; $Đ_2 << Đ_{12}$, and Eq. (40) simplifies to yield for binary mixtures

$$N_i = -\rho Đ_i \frac{q_i}{RT}\frac{d\mu_i}{dz}; \quad i = 1,2 \tag{41}$$

For an ideal gas mixture, the chemical potential gradients can be related to the partial pressure gradients in the bulk gas phase mixture

$$\frac{d\mu_i}{dz} = RT\frac{d\ln p_i}{dz} = RT\frac{1}{p_i}\frac{dp_i}{dz} \tag{42}$$

The gradients in the chemical potential can be related to the gradients of the molar loadings by defining thermodynamic correction factors Γ_{ij}

$$\frac{q_i}{RT}\frac{d\mu_i}{dz} = \sum_{j=1}^{2}\Gamma_{ij}\frac{dq_j}{dz}; \qquad \Gamma_{ij} = \frac{q_i}{p_i}\frac{\partial p_i}{\partial q_j}; \qquad i,j = 1,2 \tag{43}$$

Combination of Eqs. (41) and (43), allows us to express the fluxes explicitly in terms of the gradients of the molar loadings

$$\begin{pmatrix} N_1 \\ N_2 \end{pmatrix} = -\rho \begin{bmatrix} Đ_1 & 0 \\ 0 & Đ_2 \end{bmatrix} \begin{bmatrix} \Gamma_{11} & \Gamma_{12} \\ \Gamma_{21} & \Gamma_{22} \end{bmatrix} \begin{pmatrix} \frac{dq_1}{dz} \\ \frac{dq_2}{dz} \end{pmatrix} \tag{44}$$

The off-diagonal elements Γ_{12}, and Γ_{21} become increasingly important with increasing bulk phase pressures. As illustration, Fig. 29 presents calculations of Γ_{ij} as a function of total pressure, p_t, for binary $CO_2(1)/C_2H_6(2)$ mixture adsorption in DDR zeolite, using the mixed-gas Langmuir model (Krishna, 2016d, 2018). Except for operations in the Henry regime of adsorption, thermodynamic coupling effects cannot be ignored. Put another way, thermodynamic coupling effects arise due to non-linearities in the dependence of the component loadings within the microporous-host on the partial pressures of the components in the bulk fluid phase mixture. Both the guest molecules, CO_2, and C_2H_6 jump lengthwise across the 3.65 Å x 4.37 Å windows of DDR. Due to the smaller cross-sectional dimension of CO_2, the ratio of the M−S diffusivities of $CO_2(1)$, and $C_2H_6(2)$, $Đ_1/Đ_2$ = 1333. The transient overshoot of CO_2 is captured quantitatively by numerical simulations based on the flux Eq. (44), indicated by the continuous solid lines in Fig. 29b. The dashed lines are the corresponding simulations using a scenario in which the thermodynamic coupling effects are ignored, i.e. $\Gamma_{ij} = \delta_{ij}$. In this case, no CO_2 overshoot is observed. Broadly speaking, transient overshoots and uphill diffusion are observed for mixtures consisting of more-strongly-adsor bed-tardier-component and less-strongly-adsorbed-more-mobile-component.

For transient uptake of N_2/CH_4 mixtures, overshoots in the loading of the more mobile N_2 have been reported for LTA-4A zeolite by (Habgood, 1958); see Fig. 30a. The experimental data of (Saint-Remi et al., 2013) for transient uptake of ethanol/1-propanol mixtures within SAPO-34, that is the structural analog of CHA zeolite, are shown in Fig. 30b; the more mobile ethanol is found to exhibit a pronounced maximum during the uptake transience. The experimental data of (Titze et al., 2014) for transient uptake of *n*-hexane (nC6)/2-methylpentane(2MP) mixtures in MFI zeolite crystal, exposed to an equimolar binary gas mixture at constant total pressure, shows a pronounced overshoot in the uptake of the more mobile linear isomer nC6; see Fig. 30c. The transient overshoots, indicative of uphill diffusion in all three cases, are quantitatively captured by use of Eq. (44), and are determined to be caused by thermodynamic coupling effects (Krishna, 2016d, 2018). For zeolite catalyzed reactions, uphill diffusion and transient overshoots influence both the conversion and selectivity (Krishna et al., 2017).

Experimental data on transient permeation of CH_4/nC_4H_{10} (Geus et al., 1993), H_2/nC_4H_{10} (Bakker, 1999), nC_4H_{10}/iso-C_4H_{10} (Courthial et al., 2013), nC6/2MP (Matsufuji et al., 2000b), nC6/2,3-dimethylbutane (23DMB) (Matsufuji et al., 2000b), benzene/p-xylene (Kolvenbach et al., 2011), m-xylene/p-xylene (Matsufuji et al., 2000a) and o-xylene/m-xylene/p-xylene (Matsufuji et al., 2000a) mixtures across MFI membranes show overshoots in the flux of the more mobile partners during the transient approach towards steady-state. These flux overshoots also have their origins in thermodynamic coupling effects (Krishna, 2016d, 2017b, 2018; Krishna et al., 2018). As illustration, Fig. 31 shows the transient fluxes for permeation fluxes of 10/90 Kr/Xe across SAPO-34 membrane. During the initial transience, the Kr/Xe selectivity exceeds the steady-state value by about three orders of magnitude. The Kr flux overshoot, that is indicative of uphill diffusion (Krishna, 2015a, 2016d), disappears if the assumption $\Gamma_{ij} = \delta_{ij}$ is invoked (Krishna, 2015a, 2016d). The exploitation of transient overshoot phenomena to attain enhanced selectivities, albeit for short time durations, is a fertile area for further investigations.

16. Conclusions

The following major conclusions can be drawn from the foregoing discussions and analysis.

(1) Coupling effects in mixture diffusion are often significant, and may cause uphill transport of a species against its concentration gradient. Transient overshoots, and serpentine equilibration trajectories in composition space are fingerprints of uphill diffusion.

(2) Diffusional coupling effects cause the component Murphree efficiencies values of individual species in multicomponent distillation to be different from one another. In several cases Murphree efficiency values are unbounded and the E_i for any specific component can be either <0 or >1, indicative of uphill diffusion. Differences in the values of the component efficiencies may case the crossing of "forbidden" distillation boundaries for azeotropic mixtures.
(3) In partially miscible liquid mixtures, diffusional coupling effects become increasingly significant as the compositions approach regions in which phase splitting occurs. The coupling effects originate predominantly from the matrix of thermodynamic factors, $[\Gamma]$. Strongly coupled diffusion, and in particular uphill diffusion, is the norm, rather than the exception, in liquid extraction.
(4) Curvilinear equilibration trajectories may exhibit forays into meta-stable regions causing emulsion formation and Ouzo effect (Krishna, 2015a, 2015b). The Ouzo effect may be exploited for producing nanospheres and nanoparticles (Ganachaud and Katz, 2005).
(5) For ionic diffusion, an electro-static potential gradient is engendered due to the requirements of electro-neutrality and the no-current prescription. This additional potential gradient serves to either accelerate or decelerate an ionic species, depending on the species charge and operating conditions. For diffusion in both bulk electrolyte solutions and within ion-exchange particles, transient overshoots and uphill diffusion are routinely encountered.
(6) Forward and reverse ion exchange processes are invariably asymmetric in nature and proceed at different rates. The Helfferich *minority* rule applies for binary ion exchanges: the effective diffusivity is closer in magnitude to the ionic diffusivity of the component that is present in smaller quantity. The minority rule is the root cause of the asymmetry in the forward and reverse exchange rates.
(7) For transient uptake of mixtures within a microporous adsorbent, overshoots in loading of the more mobile partner species may occur; these are traceable to the influence of the influence of mixture adsorption thermodynamics. Transient overshoot phenomena may be exploited in diffusion-selective separations.

A recurring theme in this article is the strong influence of phase equilibrium thermodynamics on the diffusion process. Consequently, the accuracy with which uphill diffusion processes can be modeled relies heavily on the availability of accurate models to describe activity and fugacity coefficients in fluid mixtures, electrolytes, polymeric solutions and crystalline materials. Molecular simulations of both phase equilibrium and diffusion should assist in providing valuable data for reliable modeling. Efforts in this direction are already bearing fruit in the analysis of separations and reactions using zeolites and MOFs (Hansen et al., 2009, 2010; Krishna, 2009, 2012; Krishna and van Baten, 2017, 2018). Further efforts to handle complex issues such as molecular clustering (Krishna and van Baten, 2010a), and hydrogen bonding (Krishna and van Baten, 2010b) are warranted.

Appendix A. Supplementary material

Supplementary data to this article can be found online at https://doi.org/10.1016/j.ces.2018.10.032.

References

Ågren, J., 2012. Thermodynamics and diffusion coupling in alloys—application-driven science. Metall. Mater. Trans. A. 43A, 3453–3461.
Alimadadian, A., Colver, C.P., 1976. A new technique for the measurement of ternary diffusion coefficients in liquid systems. Can. J. Chem. Eng. 54, 208–213.
Arnold, K.R., Toor, H.L., 1967. Unsteady diffusion in ternary gas mixtures. A.I.Ch.E.J. 13, 909–914.
Bakker, W.J.W., 1999. Structured Systems in Gas Separation. Ph.D. Thesis, Ph.D. Dissertation. Delft University of Technology, Delft.
Bart, H.-J., 2001. Reactive Extraction. Springer-Verlag, Berlin.
Binder, T., Lauerer, A., Chmelik, C., Haase, J., Kärger, J., Ruthven, D.M., 2015. Micro-imaging of transient intracrystalline concentration profiles during two-component uptake of light hydrocarbon – carbon dioxide mixtures by DDR-type zeolites. Ind. Eng. Chem. Res. 54, 8997–9004.
Boudin, L., Götz, D., Grec, B., 2010. Diffusion models of multicomponent mixtures in the lung. ESAIM: Proc. 30, 90–103. https://doi.org/10.1051/proc/2010008.
Bres, M., Hatzfeld, C., 1977. Three-gas diffusion – experimental and theoretical study. Pflügers Arch. 371, 227–233.
Buzatu, D., Buzatu, F.D., Paduano, L., Sartorio, R., 2007. Diffusion coefficients for the ternary system water + chloroform + acetic acid at 25 °C. J. Solut. Chem. 36, 1373–1384.
Chang, H.-K., Farhi, L.E., 1973. On mathematical analysis of gas transport in the lung. Resp. Physiol. 18, 370–385.
Chang, H.-K., Tai, R.C., Farhi, L.E., 1975. Some implications of ternary diffusion in the lung. Resp. Physiol. 23, 109–120.
Chang, Y.C., Myerson, A.S., 1986. Diffusivity of glycine in concentrated solutions and supersaturated aqueous solutions. A.I.Ch.E.J. 32, 1567–1569.
Chevrolet, J.-C., 2001. Helium oxygen mixtures in the intensive care unit. Crit. Care 5, 179–181.
Chiappa, G.R., Queiroga, F., Meda, E., Ferreira, L.F., Diefenthaeler, F., Nunes, M., Vaz, M.A., Machado, M.C.L., Nery, L.E., Neder, J.A., 2009. Heliox improves oxygen delivery and utilization during dynamic exercise in patients with chronic obstructive pulmonary disease. Am. J. Respir. Crit. Care Med. 179, 1004–1010.
Christensen, N.H., 1977. Multiphase ternary diffusion couples. J. Am. Ceram. Soc. 60, 293–296.
Clark, W.M., Rowley, R.L., 1986. Ternary liquid diffusion coefficients near plait points. Int. J. Thermophys. 6, 631–642.
Courthial, L., Bandot, A., Tayakout-Fayolle, M., Jallut, C., 2013. Transient method for mass-transfer characterization through supported zeolite membranes: extension to two components. A.I.Ch.E.J. 59, 959–970.
Cullinan, H.T., Ram, S.K., 1976. Mass-transfer in a ternary liquid-liquid system. Can. J. Chem. Eng. 54, 156–159.
Cullinan, H.T., Toor, H.L., 1965. Diffusion in the three-component liquid system: acetone-benzene carbon tetrachloride. J. Phys. Chem. 69, 3941–3949.
Darken, L.S., 1949. Diffusion of carbon in austenite with a discontinuity in composition. Trans. AIME. 180, 430–438.
De Villiers, W.E., French, R.N., Koplos, G.J., 2002. Navigate phase equilibria via residue curve maps. Chem. Eng. Prog. 98 (11), 66–71.
Doherty, M.F., Malone, M.F., 2001. Conceptual Design of Distillation Systems. McGraw-Hill, New York.
Duncan, J.B., Toor, H.L., 1962. An experimental study of three component gas diffusion. A.I.Ch.E.J. 8, 38–41.
Enqvist, Y., Partanen, J., Louhi-Kultanen, M., Kallas, J., 2003. Thermodynamics and kinetics of KDP crystal growth from binary and ternary solutions. Trans. Inst. Chem. Eng. 81 (Part A), 1354–1362.
Fornasiero, F., Prausnitz, J.M., Radke, C.J., 2005. Multicomponent diffusion in highly asymmetric systems. An extended maxwell-stefan model for starkly different-sized, segment-accessible chain molecules. Macromolecules 38, 1364–1370.
Fullarton, D., Schlünder, E.U., 1986. Diffusion distillation – a new separation. Process for azeotropic mixtures – Part I: Selectivity and transfer efficiency. Chem. Eng. Process. 20, 255–263.
Fuller, E.N., Schettler, P.D., Giddings, J.C., 1966. A new method for prediction of binary gas-phase diffusion coefficients. Ind. Eng. Chem. 58, 19–27.
Ganachaud, F., Katz, J.L., 2005. Nanoparticles and nanocapsules created using the ouzo effect: spontaneous emulsification as an alternative to ultrasonic and high-shear devices. ChemPhysChem 6, 209–216.
Garside, J., 1985. Industrial crystallization from solution. Chem. Eng. Sci. 40, 3–26.
Geddes, R.L., 1946. Local efficiencies of bubble-plate fractionators. Trans. Am. Inst. Chem. Engrs. 42, 79–105.
Geus, E.R., van Bekkum, H., Bakker, W.J.W., Moulijn, J.A., 1993. High-temperature Stainless Steel Supported Zeolite (MFI) membranes: preparation, module construction, and permeation experiments. Microporous Mater. 1, 131–147.
Glicksman, M.E., 2000. Diffusion in Solids: Field Theory, Solid-state Principles, and Applications. John Wiley, New York.
Grillo, I., 2003. Small-angle neutron scattering study of a world-wide known emulsion: le pastis. Colloids Surf. A 225, 153–160.
Grossmann, T., Winkelmann, J., 2005. Ternary diffusion coefficients of glycerol + acetone + water by taylor dispersion measurements at 298.15 K. J. Chem. Eng. Data 50, 1396–1403.
Grossmann, T., Winkelmann, J., 2007a. Ternary diffusion coefficients of glycerol + acetone + water by taylor dispersion measurements at 298.15 K. 2. Acetone-rich region. J. Chem. Eng. Data 52, 336–340.
Grossmann, T., Winkelmann, J., 2007b. Ternary diffusion coefficients of glycerol + acetone + water by taylor dispersion measurements at 298.15 K. 3. Water-Rich Region. J. Chem. Eng. Data 52, 341–344.
Gupta, P.K., Cooper, A.R., 1971. The [*D*] matrix for multicomponent diffusion. Physica 54, 39–59.

Haase, M.F., Brujic, J., 2014. Tailoring of high-order multiple emulsions by the liquid-liquid phase separation of ternary mixtures. Angew. Chem. 126, 11987–11991.
Habgood, H.W., 1958. The kinetics of molecular sieve action. Sorption of nitrogen-methane mixtures by linde molecular sieve 4A. Canad. J. Chem. 36, 1384–1397.
Haeberl, M., Blass, E., 1999. Multicomponent effects in liquid-liquid extraction. Trans. I. Chem. E. 77, 647–655.
Hansen, N., Krishna, R., van Baten, J.M., Bell, A.T., Keil, F.J., 2009. Analysis of diffusion limitation in the alkylation of benzene over H-ZSM-5 by combining quantum chemical calculations, molecular simulations, and a continuum approach. J. Phys. Chem. C 113, 235–246.
Hansen, N., Krishna, R., van Baten, J.M., Bell, A.T., Keil, F.J., 2010. Reactor simulation of benzene ethylation and ethane dehydrogenation catalyzed by ZSM-5: a multiscale approach. Chem. Eng. Sci. 65, 2472–2480.
He, P., Ghoniem, A.F., 2018. Phase separation during mixing of partially miscible fluids under nearcritical and supercritical conditions, and the phenomenon of "Uphill Diffusion". J. Supercrit. Fluids 135, 105–119.
Heintz, A., Stephan, W., 1994. A generalized solution-diffusion model of the pervaporation process through composite membranes Part I. Prediction of mixture solubilities in the dense active layer using the UNIQUAC model. J. Membr. Sci. 89, 143–151.
Helfferich, F.G., 1983. Ion exchange kinetics – evolution of a theory. In: Liberti, L., Helfferich, F.G. (Eds.), Mass Transfer and Kinetics of Ion Exchange. Martinus Nijhoff Publishers, The Hague, pp. 157–179.
Jebria, A.B., 1987. Simulations of steady quaternary gas diffusion between alveolar and blood compartments. Int. J. Bio-Med. Comput. 20, 97–105.
Jebria, A.B., Bres, M., 1982. Computer simulation of ternary diffusion in distal airways. Int. J. Bio-Med. Comput. 13, 403–419.
Jones, I.L., Carta, G., 1993. Ion exchange of amino acids and dipeptides on cation resins with varying degree of cross-linking. 2. Intraparticle transport. Ind. Eng. Chem. Res. 32, 117–125.
Kolvenbach, R., Al-Yassir, N., Al-Khattaf, S.S., Gobin, O.C., Ahn, J.H., Jentys, A., Lercher, J.A., 2011. A comparative study of diffusion of benzene/p-xylene mixtures in MFI particles, pellets and grown membranes. Catal. Today 168, 147–157.
Kooijman, H.A., Taylor, R., 2007. The ChemSep Book, second ed., H.A. Kooijman and R. Taylor. www.chemsep.com.
Krishna, R., 1985. Model for prediction of point efficiencies for multicomponent distillation. Chem. Eng. Res. Des. 63, 312–322.
Krishna, R., 2009. Describing the diffusion of guest molecules inside porous structures. J. Phys. Chem. C 113, 19756–19781.
Krishna, R., 2012. Diffusion in porous crystalline materials. Chem. Soc. Rev. 41, 3099–3118.
Krishna, R., 2015a. Uphill diffusion in multicomponent mixtures. Chem. Soc. Rev. 44, 2812–2836.
Krishna, R., 2015b. Serpentine diffusion trajectories and the ouzo effect in partially miscible ternary liquid mixtures. PCCP 17, 27428–27436.
Krishna, R., 2016a. Highlighting coupling effects in ionic diffusion. Chem. Eng. Res. Des. 114, 1–12.
Krishna, R., 2016b. Highlighting diffusional coupling effects in ternary liquid extraction and comparisons with distillation. Ind. Eng. Chem. Res. 55, 1053–1063.
Krishna, R., 2016c. Investigating the validity of the knudsen diffusivity prescription for mesoporous and macroporous materials. Ind. Eng. Chem. Res. 55, 4749–4759.
Krishna, R., 2016d. Tracing the origins of transient overshoots for binary mixture diffusion in microporous crystalline materials. PCCP 18, 15482–15495.
Krishna, R., 2016e. Describing mixture permeation across polymeric membranes by a combination of maxwell-stefan and flory-huggins models. Polymer 103, 124–131.
Krishna, R., 2017a. Highlighting multiplicity in the gilliland solution to the maxwell-stefan equations describing diffusion distillation. Chem. Eng. Sci. 164, 63–70.
Krishna, R., 2017b. Using the maxwell-stefan formulation for highlighting the influence of interspecies (1–2) friction on binary mixture permeation across microporous and polymeric membranes. J. Membr. Sci. 540, 261–276.
Krishna, R., 2018. A maxwell-stefan-glueckauf description of transient mixture uptake in microporous adsorbents. Sep. Purif. Technol. 191, 392–399. https://doi.org/10.1016/j.seppur.2017.09.057.
Krishna, R., Baur, R., Van Baten, J.M., 2017. Highlighting diffusional coupling effects in zeolite catalyzed reactions by combining the maxwell-stefan and langmuir-hinshelwood formulations. React. Chem. Eng. 2, 324–336.
Krishna, R., Low, C.Y., Newsham, D.M.T., Olivera-Fuentes, C.G., Standart, G.L., 1985. Ternary mass transfer in liquid-liquid extraction. Chem. Eng. Sci. 40, 893–903.
Krishna, R., Martinez, H.F., Sreedhar, R., Standart, G.L., 1977. Murphree point efficiencies in multicomponent systems. Trans. Inst. Chem. Eng. 55, 178–183.
Krishna, R., van Baten, J.M., 2005. The Darken relation for multicomponent diffusion in liquid mixtures of linear alkanes. An investigation using Molecular Dynamics (MD) simulations. Ind. Eng. Chem. Res. 44, 6939–6947.
Krishna, R., van Baten, J.M., 2009a. An investigation of the characteristics of maxwell-stefan diffusivities of binary mixtures in silica nanopores. Chem. Eng. Sci. 64, 870–882.
Krishna, R., van Baten, J.M., 2009b. Unified Maxwell-Stefan description of binary mixture diffusion in micro- and meso- porous materials. Chem. Eng. Sci. 64, 3159–3178.
Krishna, R., van Baten, J.M., 2010a. Investigating cluster formation in adsorption of CO_2, CH_4, and Ar in zeolites and metal organic frameworks at sub-critical temperatures. Langmuir 26, 3981–3992.
Krishna, R., van Baten, J.M., 2010b. Hydrogen bonding effects in adsorption of water-alcohol mixtures in zeolites and the consequences for the characteristics of the maxwell-stefan diffusivities. Langmuir 26, 10854–10867.
Krishna, R., van Baten, J.M., 2011. A molecular dynamics investigation of the diffusion characteristics of cavity-type zeolites with 8-ring windows. Microporous Mesoporous Mater. 137, 83–91.
Krishna, R., van Baten, J.M., 2013. Investigating the influence of diffusional coupling on mixture permeation across porous membranes. J. Membr. Sci. 430, 113–128.
Krishna, R., van Baten, J.M., 2016. Describing diffusion in fluid mixtures at elevated pressures by combining the maxwell-stefan formulation with an equation of state. Chem. Eng. Sci. 153, 174–187.
Krishna, R., van Baten, J.M., 2017. Commensurate-incommensurate adsorption and diffusion in ordered crystalline microporous materials. PCCP 19, 20320–20337.
Krishna, R., van Baten, J.M., 2018. Using molecular dynamics simulations for elucidation of molecular traffic in ordered crystalline microporous materials. Microporous Mesoporous Mater. 258, 151–169. https://doi.org/10.1016/j.micromeso.2017.09.014.
Krishna, R., van Baten, J.M., Baur, R., 2018. Highlighting the origins and consequences of thermodynamic nonidealities in mixture separations using zeolites and metal-organic frameworks. Microporous Mesoporous Mater. 267, 274–292. https://doi.org/10.1016/j.micromeso.2018.03.013.
Krishna, R., Wesselingh, J.A., 1997. The maxwell-stefan approach to mass transfer. Chem. Eng. Sci. 52, 861–911.
Kuiken, G.D.C., 1994. Thermodynamics of Irreversible Processes: Applications to Diffusion and Rheology. John Wiley, Chichester, UK.
Lao, M.Z., Kingsley, J.P., Krishnamurthy, R., Taylor, R., 1989. A nonequilibrium stage model of multicomponent separation processes. 6. Simulation of liquid liquid extraction. Chem. Eng. Commun. 86, 73–89.
Lauerer, A., Binder, T., Chmelik, C., Miersemann, E., Haase, J., Ruthven, D.M., Kärger, J., 2015. Uphill diffusion and overshooting in the adsorption of binary mixtures in nanoporous solids. Nat. Commun. 6, 7697. https://doi.org/10.1038/ncomms8697.
Leahy-Dios, A., Bou-Ali, M.M., Platten, J.K., Firoozabadi, A., 2005. Measurements of molecular and thermal diffusion coefficients in ternary mixtures. J. Chem. Phys. 122, 234502.
Levy, S.G., Van Dongen, D.B., Doherty, M.F., 1985. Design and synthesis of homogeneous azeotropic distillation. 2. Minimum reflux calculations for nonideal and azeotropic columns. Ind. Eng. Chem. Fund. 24, 463–474.
Lightfoot, E.N., 1974. Transport Phenomena and Living Systems. John Wiley, New York.
Lo, P.Y., Myerson, A.S., 1989. Ternary diffusion coefficients in metastable solutions of glycine-valine-H,O. A.I.Ch.E.J. 35, 676–678.
Louhi-Kultanen, M., Kallas, J., Partanen, J., Sha, Z., Oinas, P., Palosaari, S., 2001. The influence of multicomponent diffusion on crystal growth in electrolyte solutions. Chem. Eng. Sci. 56, 3505–3515.
Matsufuji, T., Nishiyama, N., Matsukata, M., Ueyama, K., 2000a. Separation of butane and xylene isomers with MFI-type zeolitic membrane synthesized by a vapor-phase transport method. J. Membr. Sci. 178, 25–34.
Matsufuji, T., Watanabe, K., Nishiyama, N., Egashira, Y., Matsukata, M., Ueyama, K., 2000b. Permeation of hexane isomers through an MFI membrane. Ind. Eng. Chem. Res. 39, 2434–2438.
Maxwell, J.C., 1866. On the dynamical theory of gases. Phil. Trans. Roy. Soc. 157, 49–88.
Mulder, M.H.V., Smolders, C.A., 1984. On the mechanism of separation of ethanol/water mixtures by pervaporation. I. Calculation of concentration profiles. J. Membr. Sci. 17, 289–307.
Murphree, E.V., 1925. Rectifying column calculations with particular reference to n-component mixtures. Ind. Eng. Chem. 17, 747–750.
Myerson, A.S., Senol, D., 1984. Diffusion coefficients near the spinodal curve. A.I.Ch.E.J. 30, 1004–1006.
Nakagaki, M., Kitagawa, S., 1976. The theory of the reverse diffusion of ions in mixed electrolyte solutions and experimental results on the HCl-$CaCl_2$-H_2O ternary system. Bull. Chem. Soc. Jpn. 49, 1748–1753.
Newman, J., Thomas-Alyea, K.E., 2004. Electrochemical Systems. John Wiley & Sons, Inc., Hoboken, New Jersey.
Price, P.E., Romdhane, I.H., 2003. Multicomponent diffusion theory and its applications to polymer-solvent systems. A.I.Ch.E.J. 49, 309–322.
Ravi, R., 2007. Mathematical treatment of the loschmidt tube experiment: some clarifications. Chem. Eng. Commun. 194, 170–176.
Rehfeldt, S., Stichlmair, J., 2010. Measurement and prediction of multicomponent diffusion coefficients in four ternary liquid systems. Fluid Phase Equilib. 290, 1–14.
Reid, R.C., Prausnitz, J.M., Poling, B.E., 1986. The Properties of Gases and Liquids. McGraw-Hill, New York.
Reuvers, A.J., Smolders, C.A., 1987. Formation of membranes by means of immersion precipitation Part II. The mechanism of formation of membranes prepared from the system cellulose acetate – acetone – water. J. Membr. Sci. 34, 67–86.
Ribeiro, C.P., Freeman, B.D., Paul, D.R., 2011. Modeling of multicomponent mass transfer across polymer films using a thermodynamically consistent formulation of the maxwell-stefan equations in terms of volume fractions. Polymer 52, 3970–3983.

Rodriguez, J.F., Valverde, J.L., Rodrigues, A.E., 1998. Measurements of effective self-diffusion coefficients in a gel-type cation exchanger by the zero-length-column method. Ind. Eng. Chem. Res. 37, 2020–2028.
Ruschak, K.J., Miller, C.A., 1972. Spontaneous emulsification in ternary systems with muss transfer. Ind. Eng. Chem. Fundam. 11, 534–540.
Sabatier, J.P., Vignes, A., 1967. Etude des Phénomènes de Diffusion dans le Systéme Ternaire Fe-Ni-Co. Mem. Sci. Rev. Metallurg. 64, 225–240.
Saint-Remi, J.C., Baron, G.V., Denayer, J.F.M., 2013. Non-uniform chain length dependent diffusion of short 1-alcohols in SAPO-34 in liquid phase. J. Phys. Chem. C 117, 9758–9765.
Sandler, S.I., 1999. Chemical, Biochemical, and Engineering Thermodynamics. John Wiley, New York.
Seader, J.D., Henley, E.J., Roper, D.K., 2011. Separation Process Principles. John Wiley, New York.
Sethy, A., Cullinan, H.T., 1975. Transport of mass in ternary liquid-liquid systems. Part I. Diffusion studies. A.I.Ch.E.J. 21, 571–575.
Sherwood, T.K., Pigford, R.L., Wilke, C.R., 1975. Mass Transfer. McGraw-Hill, New York, U.S.A.
Sherwood, T.K., Wei, J.C., 1955. Ion diffusion in mass transfer between phases. A.I. Ch.E.J. 1, 522–527.
Shuck, F.O., Toor, H.L., 1963. Diffusion in the three component liquid system methyl alcohol – n-propyl alchohol – isobutyl alcohol. J. Phys. Chem. 67, 540–545.
Singh, N., Prasad, R., 2011. Experimental studies on the effect of inert gases on diffusion distillation of ethanol–water mixtures. J. Chem. Technol. Biotechnol. 86, 1495–1500.
Sirkar, K.K., 2014. Separation of Molecules, Macromolecules and Particles. Principles, Phenomena and Processes. Cambridge University Press, Cambridge.
Sitnikova, N.L., Sprik, R., Wegdam, G., Eiser, E., 2005. Spontaneously formed trans-anethol/water/alcohol emulsions: mechanism of formation and stability. Langmuir 21, 7083–7089.
Solans, C., Morales, D., Homs, M., 2016. Spontaneous emulsification. Curr. Opin. Colloid Interface Sci. 22, 88–93.
Springer, P.A.M., Baur, R., Krishna, R., 2002a. Influence of interphase mass transfer on the composition trajectories and crossing of boundaries in ternary azeotropic distillation. Sep. Purif. Technol. 29, 1–13.
Springer, P.A.M., Buttinger, B., Baur, R., Krishna, R., 2002b. Crossing of the distillation boundary in homogeneous azeotropic distillation: Influence of interphase mass transfer. Ind. Eng. Chem. Res. 41, 1621–1631.
Springer, P.A.M., van der Molen, S., Baur, R., Krishna, R., 2002c. Experimental verification of the necessity to use the Maxwell-Stefan formulation in describing trajectories during azeotropic distillation. Chem. Eng. Res. Des. 80, 654–666.
Springer, P.A.M., van der Molen, S., Krishna, R., 2002d. The need for using rigorous rate-based models for simulations of ternary azeotropic distillation. Comput. Chem. Eng. 26, 1265–1279.
Standart, G.L., Taylor, R., Krishna, R., 1979. The Maxwell-Stefan formulation of irreversible thermodynamics for simultaneous heat and mass transfer. Chem. Eng. Commun. 3, 277–289.
Stefan, J., 1871. Über das Gleichgewicht und die Bewegung insbesondere die Diffusion von Gasgemengen. Sitzber. Akad. Wiss. Wien. 63, 63–124.
Sun, Y., Zhao, Q., Zhang, L., Jiang, B., 2014. Measurement and correlation of the mass-transfer coefficient for the methyl isobutyl ketone−water−phenol system. Ind. Eng. Chem. Res. 53, 3654–3661.
Tai, R.C., 1979. A mathematical study of non-equimolar ternary gas diffusion. Bulletin Math. Biol. 41, 591–606.
Taveira, P., Cruz, P., Mendes, A., 2000. A Maxwell-Stefan experiment. Chem. Eng. Education. Winter, 90–93.
Taylor, R., Krishna, R., 1993. Multicomponent Mass Transfer. John Wiley, New York.
Taylor, R., Krishna, R., Kooijman, H., 2003. Real-world modeling of distillation. Chem. Eng. Prog. 99 (7), 28–39.
Titze, T., Chmelik, C., Kärger, J., van Baten, J.M., Krishna, R., 2014. Uncommon synergy between adsorption and diffusion of hexane isomer mixtures in MFI zeolite induced by configurational entropy effects. J. Phys. Chem. C 118, 2660–2665.
Tsay, C.S., McHugh, A.J., 1990. Mass transfer modeling of asymmetric membrane formation by phase inversion. J. Polym. Sci.: Part B: Polym. Phys. 28, 1327–1365.
van den Berg, G.B., Smolders, C.A., 1992. Diffusional phenomena in membrane separation processes. J. Membr. Sci. 73, 103–118.
Varshneya, A.K., Cooper, A.R., 1972. Diffusion in the system K_2O-SrO-SiO_2: III, interdiffusion coefficients. J. Am. Ceram. Soc. 55, 312–317.
Vielzeuf, D., Saúl, A., 2011. Uphill diffusion, zero-flux planes and transient chemical solitary waves in garnet. Contrib. Mineral. Petrol. 161, 683–702.
Vignes, A., 1966. Diffusion in binary solutions. Ind. Eng. Chem. Fund. 5, 189–199.
Vignes, A., Sabatier, J.P., 1969. Ternary diffusion in Fe-Co-Ni alloys. Trans. Met. Soc. A.I.M.E. 245, 1795–1802.
Vitagliano, V., Sartorio, R., Scala, S., Spaduzzi, D., 1978. Diffusion in a ternary system and the critical mixing point. J. Solut. Chem. 7, 605–621.
Vitale, S.A., Katz, J.L., 2003. Liquid droplet dispersions formed by homogeneous liquid-liquid nucleation: “The Ouzo Effect”. Langmuir 19, 4105–4110.
Vrentas, J.S., Duda, J.L., 1979. Molecular diffusion in polymer solutions. A.I.Ch.E.J. 25, 1–24.
Wankat, P.C., 2012. Separation Process Engineering. Prentice-Hall, Upper Saddle River, New Jersey, USA.
Wesselingh, J.A., Krishna, R., 2000. Mass Transfer in Multicomponent Mixtures. VSSD, Delft.
Yang, Y., Pintauro, P.N., 2000. Multicomponent space-charge transport model for ion-exchange membranes. A.I.Ch.E.J. 46, 1177–1190.
Yoshida, H., Kataoka, T., 1987. Intraparticle ion-exchange mass transfer in ternary system. Ind. Eng. Chem. Res. 26, 1179–1184.